

Primordial black hole dark matter from inflation: The reverse engineering approach

Gabriele Franciolini^{*} and Alfredo Urbano[†]

*Dipartimento di Fisica, “Sapienza” Università di Roma, Piazzale Aldo Moro 5, 00185 Roma, Italy
and INFN sezione di Roma, Piazzale Aldo Moro 5, 00185 Roma, Italy*

 (Received 13 October 2022; accepted 23 November 2022; published 23 December 2022)

Constraining the inflationary epoch is one of the aims of modern cosmology. In order to fully exploit current and future small-scale observations, it is necessary to devise tools to directly relate them to the early Universe’s dynamics. We present here a novel reverse engineering approach able to connect fundamental late-time observables to consistent inflationary dynamics and, eventually, to the inflaton potential. Employing this procedure, we are able to describe which conditions can give rise to a raised plateau in the power spectrum of curvature perturbations at small scales, which are not constrained by CMB observations. Within this new phenomenologically driven approach, we find that inflation can generate a raised plateau in the spectrum of curvature perturbations that potentially connects three fundamental observables; a dominant component of the dark matter in the form of asteroid-mass/atomic-size primordial black holes, detectable signals in stochastic gravitational waves, and a subdominant fraction of stellar-mass primordial black holes mergers.

DOI: [10.1103/PhysRevD.106.123519](https://doi.org/10.1103/PhysRevD.106.123519)

I. INTRODUCTION

The increasing accuracy of observational data relating to measurements of the cosmic microwave background (CMB) anisotropy place severe constraints on cosmic inflation. In the framework of standard single-field inflationary models with Einstein gravity, the latest results reported by the Planck and BICEP2/Keck Collaborations [1,2] imply that the predictions of slow-roll models with a concave potential are strongly favored by data and no evidence for dynamics beyond slow-roll was found. On the theoretical side, these constraints have far-reaching implications. For instance, a simple inspection of the theoretical predictions regarding the power spectra of scalar and tensor perturbations leads to the conclusion that the standard version of natural inflation and the full class of monomial potentials $V(\phi) \sim \phi^n$ are now strongly disfavored [3].

However, it is important to keep in mind that the above discussion is limited only to a relatively short part of the inflationary dynamics, namely the one that took place at around 60 e -folds before the end of inflation when curvature perturbations with comoving wave number in the range $0.005 \lesssim k [\text{Mpc}^{-1}] \lesssim 0.2$ exited the Hubble horizon. On smaller scales (larger k), the observational constraints are far weaker implying that deviations from the slow-roll paradigm are possible; consequently, claiming

any theoretical control over the inflationary potential is, at these scales, way more difficult.

Deviations from slow-roll dynamics at small scales may have interesting consequences as far as the formation of primordial black holes (PBHs) is concerned [4–7]. In the inflationary picture, spacetime fluctuates quantum mechanically around a background that is expanding exponentially fast; after the end of inflation, these curvature fluctuations are transferred to the radiation field, creating slightly over and underdense regions. Regions where the overdensity is large enough, gravitationally collapse and form PBHs [8–11]. At the practical level, the implementation of this idea requires some mechanism that boosts, at scales relevant for PBH formation, the power spectrum of curvature fluctuations $P_{\mathcal{R}}(k)$ way above the value inferred from CMB observations [that is, $P_{\mathcal{R}}(k_*) \approx 2 \times 10^{-9}$ with $k_* \equiv 0.05 \text{ Mpc}^{-1}$ the CMB pivot scale] and necessarily breaks the slow-roll paradigm [12]. A popular option is the introduction of an ultraslow-roll (USR) phase during the inflationary dynamics. At the classical level, during USR the inflaton nearly stops its descent along the potential and remains for a long interval of time with almost zero velocity before reaccelerating towards the end of inflation. At the quantum level, during USR comoving curvature perturbations on superhorizon scales are not conserved and are subject to exponential growth due to the presence of a negative friction term in their equation of motion. It is precisely this exponential enhancement that provides the above mentioned boost in the power spectrum of scalar perturbations. The simplest option to get such dynamics is

^{*}gabriele.franciolini@uniroma1.it.

[†]alfredo.urbano@uniroma1.it.

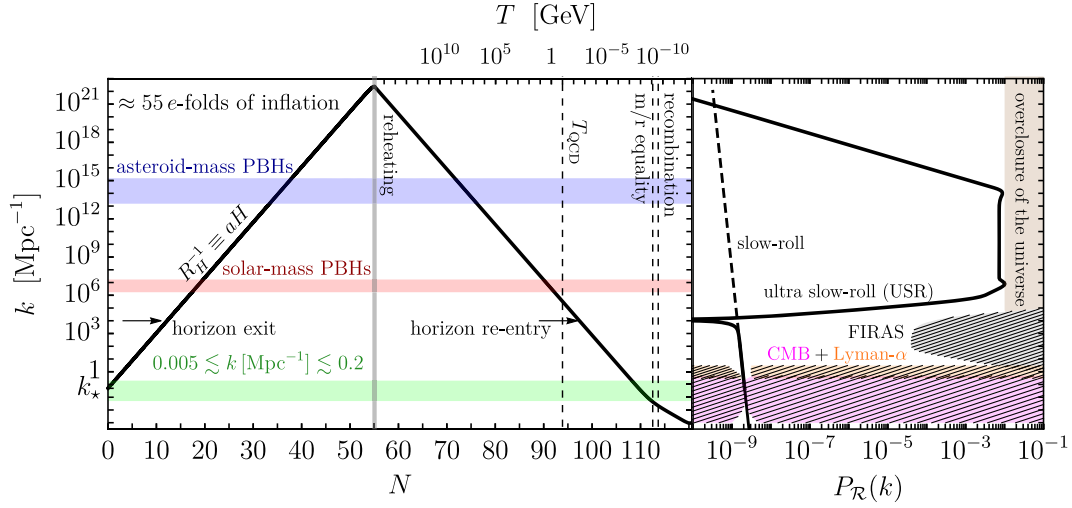


FIG. 1. (left) Time evolution (in terms of the number of e -folds N defined by $dN = Hdt$) of the inverse comoving Hubble horizon $R_H^{-1} \equiv aH$ throughout the history of our observable Universe. We start from $N = 0$, defined as the time at which the CMB pivot scale $k_* = 0.05 \text{ Mpc}^{-1}$ crossed the Hubble horizon, $k_* = a(0)H(0)$. We assume instantaneous reheating and, after inflation, standard Λ CDM cosmology. The three horizontal bands mark the milestones of our phenomenological analysis. The region shaded in green ($0.005 \lesssim k [\text{Mpc}^{-1}] \lesssim 0.2$) represents the range of comoving wave numbers with constant k in the figure) constrained by CMB anisotropy measurements, the region shaded in red ($1.7 \times 10^6 \lesssim k [\text{Mpc}^{-1}] \lesssim 1.7 \times 10^7$) corresponds to the range of comoving wave numbers for which curvature perturbations, after reentering the cosmological horizon, have the chance of generating solar-mass PBHs ($1 \lesssim M_{\text{PBH}}[M_\odot] \lesssim 100$), and the region shaded in blue ($1.5 \times 10^{13} \lesssim k [\text{Mpc}^{-1}] \lesssim 1.5 \times 10^{14}$) is the same as the red band but corresponds to asteroid-mass PBHs ($10^{-16} \lesssim M_{\text{PBH}}[M_\odot] \lesssim 10^{-12}$). Right part. We plot the power spectrum of scalar perturbations $P_{\mathcal{R}}(k)$ as a function of the comoving wave number k . The plot is rotated in such a way as to share the same y-axis with the left part of the figure. We plot the region excluded by CMB anisotropy measurements, Ref. [1], the FIRAS bound on CMB spectral distortions, Ref. [29] and the bound obtained from Lyman- α forest data [30]. If $P_{\mathcal{R}}(k) \gtrsim 10^{-2}$ the abundance of PBHs overcloses the Universe (that is, their abundance would be larger than the cold dark matter density of the Universe). The black dashed line is the typical prediction of slow-roll inflationary models. The solid black line, on the contrary, is characterized by the presence of an USR phase [concretely, it corresponds to model (1) in Sec. II and Ref. [31]].

to consider an inflationary potential that features (after the first flattish region that ensures the slow-roll dynamics needed for the fit of CMB measurements) an approximate stationary inflection point.

The cosmological setup we have in mind is summarized in Fig. 1 (see caption for details). Observational data force the curvature power spectrum (that we plot in the right panel of Fig. 1) to have, in the range $0.005 \lesssim k [\text{Mpc}^{-1}] \lesssim 0.2$, a power law functional form of the type $P_{\mathcal{R}}(k) = A_s(k/k_*)^{n_s-1}$, with amplitude $A_s \simeq 2.1 \times 10^{-9}$ and spectral index $n_s \simeq 0.965$, which fits extremely well the typical outcome of slow-roll inflationary models (black dashed line in the right panel of Fig. 1). However, if we consider larger k an almost uncharted territory opens up, and huge deviations from the slow-roll paradigm are possible. The solid black line in the right panel of Fig. 1 differs from the dashed line because of the presence of an USR phase. In this respect, Fig. 1 summarizes the main objectives of the present work. We are interested in curvature power spectra that feature, because of USR, a raised plateau at small scales which are not constrained by CMB observations. We impose three phenomenological requirements;

- (i) The part of the power spectrum at large scales (that is, for comoving wave numbers corresponding to the horizontal green band in the left panel of Fig. 1) must be consistent with CMB observations.
- (ii) The left-side edge of the plateau (that is, at small k) corresponds to values of k for which curvature perturbations re-enter the cosmological horizon when the latter has a mass of the order of the solar mass (the horizontal red band in the left panel of Fig. 1). This is to generate a sizable abundance of solar-mass PBHs. This is an interesting phenomenological requirement since it implies the possibility that a fraction of merger events directly observed by the LIGO/Virgo/KAGRA Collaboration (LVKC) is (or will be) ascribable to stellar-mass PBHs [13,14]. We remark that the red band reenters the cosmological horizon when the temperature of the Universe (labels on the upper x -axis) is of the order of the QCD quark-hadron phase transition (in Fig. 1 taken to be $T_{\text{QCD}} = 0.1 \text{ GeV}$).

The right-side edge of the plateau (that is, at large k) corresponds to values of k for which curvature perturbations reenter the cosmological horizon when

the latter has a mass of the order of the asteroid mass (the horizontal blue band in the left panel of Fig. 1). This is to generate a sizable abundance of asteroid-mass PBHs.

- (iii) We take the amplitude of the plateau to be as close as possible to the allowed upper limit, $P_{\mathcal{R}}(k) = O(10^{-2})$. This is to generate an abundance of asteroid-mass PBHs compatible with the observed dark matter (DM) content of the Universe.

As well known, an interesting byproduct of (ii) and (iii) is the possibility to generate a stochastic signal of gravitational waves (GWs) that are induced, as a second-order effect, by curvature perturbations [15–20] (see Ref. [21] for a recent review). The frequency f is related to the comoving wave number k by the relation $k \simeq 7 \times 10^{14} (f/\text{Hz}) \text{Mpc}^{-1}$ so that the two sides of the plateau in Fig. 1 correspond to $f = O(0.1)$ Hz (the typical target of future space-based GW interferometers like LISA [22–24]) and $f = O(10^{-9})$ Hz (the typical target of Pulsar Timing Array (PTA) experiments). Interestingly, the NANOGrav Collaboration has recently published an analysis of 12.5 yrs of pulsar timing data reporting a strong evidence for a stochastic common process, potentially induced by a SGWB, at a frequency of $O(10^{-9} \text{ Hz})$ [25] (also independently supported other by PTA experiments [26–28]).

The presence of the plateau in the power spectrum opens the possibility to connect all the above observables even if characterized by widely different scales. In Ref. [32] it was indeed shown that a broad power spectrum in the form of a simple double-Heaviside theta function $P_{\mathcal{R}}(k) = A\Theta(k - k_{\min})\Theta(k_{\max} - k)$ with endpoints $k_{\min} \simeq 10^{-9}k_{\max}$ and $k_{\max} \simeq 10^{15} \text{Mpc}^{-1}$ and amplitude $A = 5.8 \times 10^{-3}$ has the chance to produce the observed abundance of DM in the form of PBHs and, at the same time, generate a GW signal compatible (in frequency and amplitude) with the NANOGrav signal. In this paper, we will explicitly derive the inflationary dynamics required to realize an analogous power spectrum, revealing the much richer phenomenology associated with this scenario.

To be more specific, the solid black line in the right panel of Fig. 1 corresponds to one of the USR models recently constructed in Ref. [31]. The analysis of Ref. [31] is based on what is called a “reverse engineering approach” (see Refs. [33–36] for a similar viewpoint). The idea that lies at the heart of this approach is that the starting point of the analysis is not the inflaton potential but rather the inflationary dynamics. Let us motivate this change of perspective. As mentioned above, the presence of an USR phase in the inflationary dynamics can be obtained if one takes a scalar potential that features an approximate stationary inflection point. The latter is usually controlled by a number of free parameters that need to be fine-tuned up to very special values in order to guarantee the desired enhancement in the power spectrum of curvature perturbations [37–49]. At the technical level, this operation is not

very transparent in the sense that it is typically difficult to isolate which parameters in the scalar potential control some specific feature of the power spectrum. In the approach of Ref. [31] the scalar potential is nothing but an outcome of the analysis which, on the contrary, puts in the foreground the inflationary dynamics starting from an analytical ansatz for the Hubble parameter η . As a result, the construction of inflationary models that give curvature power spectra with features compatible with the phenomenological requirements enumerated above becomes, at the technical level, far way accessible and, from the point of view of the physics involved, more transparent.

Let us stress the following important conceptual point. Applying the reverse engineering approach of Ref. [31] would be almost meaningless if one were only interested in the part of the power spectrum constrained by CMB observations. The reason is that, as mentioned at the very beginning of this introductory discussion, at CMB scales the experimental constraints are so tight that they almost completely nail down, at the corresponding field values, the form of the inflationary potential and a detailed analysis of specific models is possible. This is not true, however, if one is interested in the behavior of the power spectrum at much smaller scales where, as illustrated in Fig. 1, observational constraints are weaker and deviations from the slow-roll paradigm possible. In this case, contrary to what happens in the reverse engineering approach of Ref. [31], there is no clear mapping between the free parameters of the scalar potential and the phenomenological implications that the presence of an USR phase may have.

The purpose of this work is to deepen the analysis presented in Ref. [31], and we organize our material as follows. In Sec. II we clarify the details of the reverse engineering approach by carefully describing the steps used to compute the spectrum of perturbations starting from the inflationary dynamics with a special emphasis on explaining with analytical arguments the mechanism that generates the plateau in the power spectrum as well as the physical meaning of the free parameters describing the inflationary dynamics. In Sec. III we review the computation of the PBH abundance. In Sec. IV we discuss the implications for the scalar-induced GW signal. In Sec. V we give more details about the profile of the reconstructed inflationary potential and its theoretical interpretation. Finally, we conclude in Sec. VI.

Throughout this paper, we use natural units and set the reduced Planck mass to unity.

II. BACKGROUND EVOLUTION AND SPECTRUM OF CURVATURE PERTURBATIONS

In this section we introduce the bases of our reverse engineering approach. We start with a parametrized background Hubble evolution, followed by the computation of curvature perturbations and an in-depth discussion of the

characteristic features leading to the important phenomenological signatures presented in the following sections.

A. Background evolution

The inflationary background can be described by modelling the evolution of the Hubble rate H . This is dictated by dynamical equations relating H to the Hubble parameters, which are

$$\epsilon \equiv -\frac{\dot{H}}{H^2}, \quad \eta \equiv -\frac{\ddot{H}}{2H\dot{H}} = e^{-\frac{1}{2} \frac{d \log \epsilon}{dN}}, \quad (1)$$

where $\dot{H} = dH/dt$ is the cosmic-time derivative of H while N , defined such as $dN = Hdt$, is the number of e -folds. One can notice that, if we assume ϵ to be small and η constant, Eq. (1) admits the solution $\epsilon(N) \propto e^{-2\eta N}$. As we will see in the following, this behavior leads to an exponential enhancement of the amplitude of perturbations when the dynamics is characterized by large and positive η , as it is the case in an USR phase.

We base our construction on an analytical ansatz for the time evolution of η of the form

$$\eta(N) = \frac{1}{2} \left\{ \left[\eta_I - \eta_{II} + (\eta_{II} - \eta_I) \tanh\left(\frac{N - N_I}{\delta N_I}\right) \right] + \left[\eta_{II} + \eta_{III} + (\eta_{III} - \eta_{II}) \tanh\left(\frac{N - N_{II}}{\delta N_{II}}\right) \right] + \left[\eta_{IV} - \eta_{III} + (\eta_{IV} - \eta_{III}) \tanh\left(\frac{N - N_{III}}{\delta N_{III}}\right) \right] \right\}. \quad (2)$$

The consequent behavior of $\epsilon(N)$ that follows from such ansatz is derived by directly integrating the differential Eq. (1). The reasons that leads to the specific ansatz presented in Eq. (2) will become clear in the following. The inflationary dynamics can be divided into four subsequent stages, as we also show in Fig. 2:

- (i) We fix the initial time at N_{ref} and an initial small value of ϵ_I . As long as the number of e -folds falls within the interval $N \in [N_{\text{ref}}, N_I]$, the ansatz forces η_I to remain constant and negative; the solution of Eq. (2), predicting a scaling of the form $\epsilon(N) \propto e^{-2\eta N}$, give rise to an exponential variation of ϵ during this phase. However, as the value of η_I is taken to be small (with the aim of reproducing the conventional slow-roll dynamics), the evolution of ϵ is tamed.
- (ii) Within the subsequent interval $N \in [N_I, N_{II}]$ we impose $\eta_{II} > (3 + \epsilon)/2 \simeq 3/2$. A negative value of η is associated to a period of negative friction, and the Hubble parameter ϵ is forced to decrease abruptly down to values $O(\ll \epsilon_I)$. This phase realists the ultraslow-roll (USR) evolution typically advocated

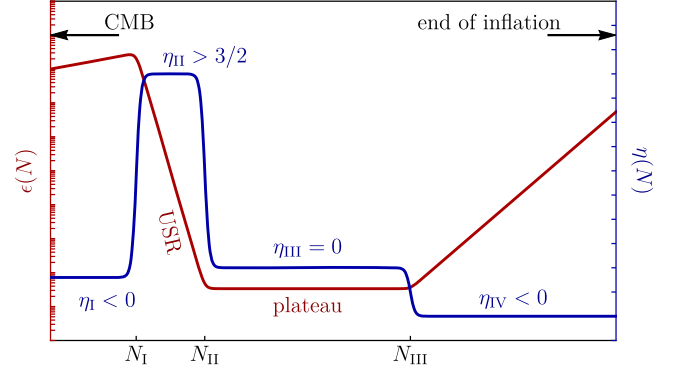


FIG. 2. Schematic evolution of $\eta(N)$ and $\epsilon(N)$. The former is given by our analytical ansatz in Eq. (2); the latter follows from Eq. (1). We label the USR phase characterized by a negative friction and the plateau in ϵ in the phase of vanishing η_{III} .

to generate enhanced spectra at small scales, within single field models of inflation.

- (iii) Subsequently, when the number of e -folds falls within $N \in [N_{II}, N_{III}]$, impose $\eta_{III} = 0$. This forces ϵ to remain constant at the tiny value reached at the end of the negative friction phase.
- (iv) The final phase is characterized by $\eta_{IV} < 0$, which is a necessary requirement to bring ϵ back to $O(1)$ values and cause the end of inflation.

The sharpness of the transition between each phase is controlled by the parameters $\delta N_{I,II,III}$. In the limit of vanishing $\delta N \rightarrow 0$, one obtains step transitions which are, however, unphysical. The expectations about the time evolution of ϵ qualitatively described above are confirmed by solving numerically Eq. (1), adopting the parametrization of $\eta(N)$ and using the initial condition $\epsilon(N_{\text{ref}}) = \epsilon_I$ imposed at the initial reference time N_{ref} . The solution is shown in Fig. 2 assuming the parameters reported in Table I. As we will see in the following, the free parameters entering in the ansatz (2) will have a clear and direct connection to physical observables (as highlighted in Table I below) and can be adjusted to devise consistent inflationary dynamics producing interesting late time signatures. We will come back to this point later on.

B. Model parameters

In the following, we shall discuss in detail the free parameters entering in Eq. (2), whose interpretation is summarized in Table I.

- (i) The values of the parameters ϵ_I , η_I , and V_{ref} are fixed by requiring consistency with large scale CMB observations. In our model, this constraint is simply fulfilled by the dynamics of the first phase before N_{ref} extending backwards up to CMB scales. We define $k_{\text{ref}} = 0.05 \text{ Mpc}^{-1}$ as the scale that exits the Hubble horizon at time N_{ref} , that is the CMB pivot scale [1], and use the slow-roll relations

TABLE I. Free parameters of our model together with their numerical benchmark values. We define $\Delta N_{\text{USR}} \equiv N_{\text{II}} - N_{\text{I}}$ and $\Delta N_{\text{plateau}} \equiv N_{\text{III}} - N_{\text{II}}$. Dimensionful quantities are written in units of the reduced Planck mass. $\delta N_{\text{I}} = 0.50$ is kept fixed.

Model parameter	Model (1)	Model (2)	Model (3)	Spectral feature	Phenomenology
ϵ_{I}		3.125×10^{-4}		Tilt of $P_{\mathcal{R}}$ at CMB scales	n_s, r
η_{I}		-1.68×10^{-2}			
V_{ref}		1.55×10^{-10}		Amplitude of $P_{\mathcal{R}}$ at CMB scales	A_s
N_{ref}		0		Pivot scale k_*	CMB
N_{I}		15.5		Large-scale edge of the plateau k_{min}	Solar-mass PBHs
δN_{II}	0.50	0.46	0.60	Bump at k_{min}	Peak of solar-mass PBHs
η_{II}	2.709	2.710	2.735	Height of the plateau	PBH = DM: $f_{\text{PBH}} = 1$
ΔN_{USR}		2.9			
η_{III}		0		Plateau	Multi-scales $\Omega_{\text{GW}}(f)$ signal
$\Delta N_{\text{plateau}}$		16.6		Small-scale edge of the plateau k_{max}	Asteroid-mass PBHs
δN_{III}	0.50	0.50	1.31	Bump at k_{max}	Peak of asteroid-mass PBHs
N_{IV}		55		Drop-off	End of inflation
η_{IV}	-0.554	-0.554	-0.560		

$$\eta_{\text{I}} = (n_s - 1 + 4\epsilon_{\text{I}})/2 \quad \text{and} \quad \epsilon_{\text{I}} = r/16, \quad (3)$$

linking the Hubble parameters at the pivot scale with the scalar spectral index n_s and the tensor-to-scalar ratio r . In other words, we anchor the initial values η_{I} and ϵ_{I} to CMB observables. Moreover, the amplitude of the power spectrum at the pivot scale, A_s , is related (via H^2) to V_{ref} by means of the Friedmann equation. We find

$$V_{\text{ref}} = 24\pi^2 \epsilon_{\text{I}} (1 - \epsilon_{\text{I}}/3) A_s. \quad (4)$$

We fix n_s , A_s , and r consistently with observations at CMB scales (with the value of r within reach in next-generation CMB measurements). This, in turn, will directly nail down the fundamental parameters ϵ_{I} , η_{I} , and V_{ref} of our phenomenological model [50]. For definiteness, we take $n_s = 0.965$, $r = 0.005$ and $A_s = 2.1 \times 10^{-9}$ [1].

- (ii) The value of N_{I} sets the beginning of the USR phase and controls the comoving wave number at which the power spectrum of curvature perturbations starts increasing with respect to its slow-roll value. In order to reproduce the results of Ref. [32], we need an early growth of the power spectrum at scales set by the value of k_{min} . As a rule of thumb, we estimate the corresponding value of N_{I} by means of the logarithmic scaling

$$N_{\text{I}} \simeq \log\left(\frac{k_{\text{min}}}{k_*}\right). \quad (5)$$

The above estimate represents a first guess for N_{I} around which we tune its final value by the accurate solving of the Mukhanov-Sasaki (MS) equation.

- (iii) The values of η_{II} and $\Delta N_{\text{USR}} \equiv N_{\text{II}} - N_{\text{I}}$ control the height of the plateau in the power spectrum. These values are tuned in order to get the right abundance of dark matter in the form of PBHs.
- (iv) We set $\eta_{\text{III}} = 0$ in order to generate a plateau in the power spectrum.
- (v) The e -fold interval $\Delta N_{\text{plateau}} \equiv N_{\text{III}} - N_{\text{II}}$ controls the broadness of the plateau. In order to reproduce the results of Ref. [32] we need a broad plateau that covers approximately the range of comoving wave numbers $k_{\text{max}}/k_{\text{min}} \approx 10^9$. As a rule of thumb, we estimate the corresponding value of $\Delta N_{\text{plateau}}$ by means of the logarithmic scaling

$$\Delta N_{\text{plateau}} \equiv N_{\text{III}} - N_{\text{II}} \simeq \log\left(\frac{k_{\text{max}}}{k_{\text{min}}}\right). \quad (6)$$

The above estimate represents a first guess for $\Delta N_{\text{plateau}}$ around which we tune its final value by the accurate solving of the MS equation.

- (vi) We fix $N_{\text{IV}} = 55$ in order to get a long enough inflationary phase to solve the horizon and flatness problems. Consequently, the value of η_{IV} is tuned in order to get $\epsilon = 1$ at $N_{\text{IV}} = 55$.
- (vii) The parameters $\delta N_{\text{I,II,III}}$ control the sharpness of the transitions in the evolution of $\eta(N)$ at e -fold times, respectively, N_{I} , N_{II} , and N_{III} . The limit $\delta N \rightarrow 0$ corresponds to a step transition. In short, these parameters control the bumplike features that are present in the power spectrum at the two edges of the plateau region (see the detailed discussion in Sec. II E). These parameters, therefore, play a very special role in our analysis. This is because the computation of the PBH abundance is exponentially sensitive to the shape of the power spectrum, and small variations are capable of producing very sizable effects.

C. Curvature perturbations

Once the background evolution is specified, one can compute the spectrum of gauge-invariant comoving curvature perturbation generated during inflation and transferred to the radiation fluid after reheating. As long as the slow-roll approximation is valid, this can be computed as

$$P_{\mathcal{R}}(k) = \frac{H^2}{8\pi^2\epsilon}, \quad (7)$$

where the Hubble parameters are evaluated at horizon crossing of modes k . To get an expectation of what spectrum of curvature perturbations would result from Eq. (2), one could naively reverse the evolution of ϵ shown in Fig. 2, that clearly features an exponential growth followed by a plateau region inherited from the term $1/\epsilon$.

In order to confirm this intuition beyond the slow-roll approximation, we compute $P_{\mathcal{R}}(k)$ by solving the MS equation [51,52]

$$\frac{d^2 u_k}{dN^2} + (1 - \epsilon) \frac{du_k}{dN} + \left[\frac{k^2}{(aH)^2} + (1 + \epsilon - \eta)(\eta - 2) - \frac{d}{dN}(\epsilon - \eta) \right] u_k = 0, \quad (8)$$

which was shown to describe the properties of perturbations at the linear level even with the inclusion of quantum diffusion effects [53]; it should be noted, however, that stochastic effects may become relevant, beyond the linear order, during the USR phase [54–58]. We remark that we do not include in our analysis any nonlinear effects related to the dynamics of curvature perturbations (e.g., [59–63]). Non-Gaussian effects, for a given mode k , are mostly controlled by the value of η after the mode settles to its final conserved value [64–66]. Modes that contribute to the plateau become constant during phase (iii) with $\eta_{\text{III}} = 0$ and, therefore, should have negligible non-Gaussianity. Modes that contribute to the right-side edge and the subsequent fall-off of the power spectrum, settle to their final constant value during phase (iv) with η_{IV} nonzero and negative. However, in all realizations of our model we consider in this work (see Table I) the actual value of $|\eta_{\text{IV}}|$ is small, and we do not expect large corrections [67] (reabsorbable by a small retuning of η_{II}). Furthermore, we model the transitions at the beginning and end of the USR phase in a smooth way, and this has the effect of further suppress local non-Gaussianity [61,62]. Finally, assessing the impact of nonlinear stochastic effects on our model deserves a separate analysis beyond the scope of this work.

We solve the MS equation with subhorizon Bunch-Davies initial conditions at $N \ll N_k$, where N_k indicates the horizon crossing time for the mode k , that is the time at which we have $k = a(N_k)H(N_k)$. This is implemented as

$$u_k(N \ll N_k) = \frac{1}{\sqrt{2k}},$$

and

$$\frac{du_k(N \ll N_k)}{dN} = -\frac{k}{\sqrt{2}a(N)H(N)}, \quad (9)$$

where, without loss of generality, we choose the phase of u_k such that it is real initially. We then compute the power spectrum $P_{\mathcal{R}}(k)$ of the gauge-invariant comoving curvature perturbation \mathcal{R} given by

$$P_{\mathcal{R}}(k) = \frac{k^3}{2\pi^2} \left| \frac{u_k(N)}{z(N)} \right|_{N > N_{\text{F}}(k)}^2,$$

with

$$\mathcal{R}_k(N) = -\frac{u_k(N)}{z(N)},$$

and

$$z(N) = a(N) \frac{d\phi(N)}{dN}. \quad (10)$$

In Eqs. (8) and (10) $\mathcal{R}_k(N)$ and $u_k(N)$ are time-dependent Fourier mode corresponding to a fixed comoving wave-number $k \equiv |\vec{k}|$. The power spectrum $P_{\mathcal{R}}(k)$ does not depend on time because the meaning of Eq. (10) is that $P_{\mathcal{R}}(k)$ must be evaluated after the time $N_{\text{F}}(k)$ at which the mode $|u_k(N)/z(N)|$ freezes to the constant value that is conserved until its horizon reentry. We then have

$$N_{\text{F}}(k) \equiv \max\{N_k, N_{\text{II}}\}. \quad (11)$$

Modes that exit the horizon *before* the time N_{II} (that is modes such that $N_k < N_{\text{II}}$) are not conserved (even though superhorizon) because they experience afterward the negative friction phase. Consequently, for these modes their contribution to Eq. (10) must be evaluated at any time $N > N_{\text{II}} > N_k$ after the negative friction phase ends. Contrariwise, modes that exit the horizon *after* the time N_{II} (that is modes such that $N_k > N_{\text{II}}$) freeze to their constant value after they become superhorizon. Consequently, as customary, the contribution of these modes to Eq. (10) must be evaluated at any time $N > N_k > N_{\text{II}}$.

It is sometime useful to rewrite the MS equation in the form

$$\frac{d^2 \mathcal{R}_k}{dN^2} + (3 + \epsilon - 2\eta) \frac{d\mathcal{R}_k}{dN} + \frac{k^2}{(aH)^2} \mathcal{R}_k = 0. \quad (12)$$

Assuming $\epsilon \approx 0$, constant η and constant H , this equation admits the solution

$$\mathcal{R}_k(N) \propto e^{-\left(\frac{3}{2} - \eta\right)N} \left[c_1 J_{\frac{3}{2} - \eta} \left(\frac{k}{k_*} e^{-N} \right) \Gamma \left(\frac{5}{2} - \eta \right) + c_2 J_{-\frac{3}{2} + \eta} \left(\frac{k}{k_*} e^{-N} \right) \Gamma \left(-\frac{1}{2} + \eta \right) \right], \quad (13)$$

where $J_\alpha(x)$ are Bessel functions of the first kind and $\Gamma(x)$ is the Euler gamma function. We are interested in the

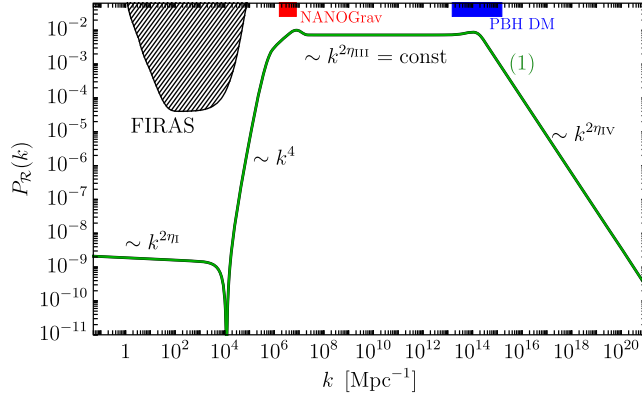


FIG. 3. Power spectrum (solid green) corresponding to the model described in the second column of Table I. The region shaded in gray corresponds to the region constrained by CMB spectral distortions [29]. To guide the eye, we indicate in red the frequency range $2.5 \times 10^{-9} < f$ [Hz] $< 1.2 \times 10^{-8}$ characterising the NANOGrav signal and in blue the mass range $10^{-16} < M_{\text{PBH}}[M_{\odot}] < 10^{-12}$ in which PBHs may comprise the totality of DM.

sub-Hubble regime, meaning that in the argument of the Bessel function $ke^{-N}/k_{*} \gg 1$. In this limit the asymptotic behavior of the Bessel function is controlled, at the first order, by the scaling $J_{\alpha}(x) \sim 1/\sqrt{x}$.

We show the numerical result of this procedure in Fig. 3. During the transition from the initial slow-roll phase to the plateau, we note that our model gives the steepest growth $\sim k^4$ [68]. The numerical solution of the MS equation in Fig. 3 shows that the USR dynamics encoded in Eq. (2) correctly gives a plateau in the power spectrum of curvature perturbations that is compatible with the result of Ref. [32]. The numerical values of the parameters used in Fig. 3 are summarized in Table I (second row).

Two aspects of our approach are truly remarkable. First, all free parameters entering in Eq. (2) have a neat and simple relation to a physical observable; this is summarized in the last two columns of Table I, and discussed in full detail in the following sections. This is contrary to what usually happens if one takes the conventional route of starting from the potential and then studying the dynamics. The free parameters entering the scalar potential usually give very little intuition about the physics of PBH formation. Second, our analysis is not just a mere rewording of what done in Ref. [32]; on the contrary, our approach discloses a much richer phenomenology that we shall now discuss. Furthermore, it will allow us to derive the inflationary potential that realise such scenario.

D. On the formation of a raised plateau in the power spectrum

The modes that form the plateau are those that exit the horizon during the phase $N_{\text{II}} < N < N_{\text{III}}$ with $\eta = 0$. We show in Fig. 4 the time evolution of three representative

modes of this kind for which $N_{\text{II}} < N_k < N_{\text{III}}$. We shall analyze the dynamics in three subsequent steps, and arrive at a simple analytical understanding of the plateau's formation.

- (i) $N < N_{\text{I}}$. The modes are sub-Hubble ($k \gg aH$). The modulus of the function $k^{3/2}|u_k(N)/z(N)|$ exponentially decays while its real and imaginary parts oscillate. For different k , the modes decay equally fast (see left panel of Fig. 4). Using Eq. (13) and neglecting η since $|\eta_{\text{I}}| \ll 1$, we simply have $k^{3/2}|u_k(N)/z(N)| \sim e^{-N}$. This time dependence is confirmed numerically in Fig. 4.

The difference in normalization—the function $k^{3/2}|u_k(N)/z(N)|$ is bigger for larger k , see left panel of Fig. 4—can be traced back to the Bunch-Davies initial condition. Deep in the sub-Hubble regime, we have

$$k^{3/2} \left| \frac{u_k(N)}{z(N)} \right| \sim k^{3/2} \times \frac{1}{\sqrt{k}} = k. \quad (14)$$

Since the subsequent time evolution is universal, we conclude that the difference between two modes with comoving wave numbers k_1 and $k_2 < k_1$ is simply given by k_1/k_2 as a consequence of Eq. (14). This is confirmed numerically if we compare the modes with $k_{1,2,3}$ (that differ between each other by one order of magnitude) displayed in the left panel of Fig. 4.

- (ii) $N_{\text{I}} < N < N_{\text{II}}$.

The modes enter in the negative-friction phase, and they are now exponentially enhanced. The key point is that modes with different k experience, during this phase, the same amount of exponential growth. The latter is fixed by the value of η_{II} and the duration of the negative-friction phase $\Delta N_{\text{USR}} = N_{\text{II}} - N_{\text{I}}$ [47]. This is again a consequence of Eq. (13); since $\eta_{\text{II}} > 3/2$, the factor $e^{-(3/2-\eta)N}$ gives an exponential growth that is bigger for longer ΔN_{USR} . Consequently, at the end of the negative-friction phase modes with different k_1 and $k_2 < k_1$ will still differ between each other by the factor k_1/k_2 . This is confirmed numerically if we compare at $N = N_{\text{II}}$ the modes with $k_{1,2,3}$ in the left panel of Fig. 4.

- (iii) $N_{\text{II}} < N < N_{\text{III}}$.

The modes exit from the negative friction phase. The function $k^{3/2}|u_k(N)/z(N)|$ decays exponentially fast in the sub-Hubble regime until the time $N = N_k$ at which the mode crosses the Hubble horizon and settles to its final constant value. During this phase the time-dependence is again given by

$$k^{3/2} \left| \frac{u_k(N)}{z(N)} \right| \sim e^{-N}. \quad (15)$$

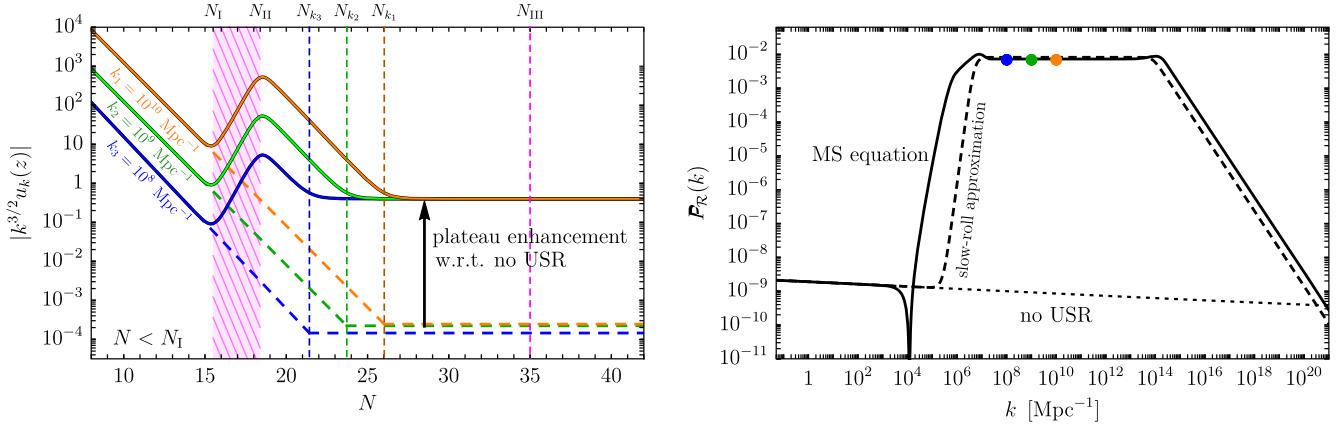


FIG. 4. Time evolution (in terms of the e -fold number) of $k^{3/2}|u_k(N)/z(N)|$ for three different modes with $k_{1,2,3} = 10^{10,9,8} \text{ Mpc}^{-1}$ obtained by numerically solving the MS equation (solid lines). The dashed lines correspond to the absence of the USR phase. The vertical lines labeled with N_k mark the e -fold time of horizon crossing for the mode with comoving wave number k . As shown in the right panel (colored dots, one for each $k_{1,2,3}$), these modes contribute to the plateau of the power spectrum. In this plot we also show the power spectrum corresponding to the absence of the USR phase (dotted) and the one computed by means of the slow-roll approximation (dashed).

This follows from the time dependence of Eq. (13) with $\eta_{III} = 0$. The key point is that now the value of N_k is larger for increasing k since we have $N_k = \log(k/k_*)$. This means that modes with different k_1 and $k_2 < k_1$ will experience, before horizon crossing, a different amount of exponential suppression; the mode with $k_1 > k_2$ will exit the horizon after the k_2 mode. Consequently, the k_1 mode will get, compared to the k_2 mode, an extra suppression given by the factor

$$e^{-\log(k_1/k_2)} = \frac{k_2}{k_1}. \quad (16)$$

This extra suppression will precisely cancel the initial enhancement of the k_1 mode compared to the k_2 mode, as discussed below Eq. (14), so that they eventually settle precisely on the same value. This compensating mechanism produces the plateau. It should be stressed that this exact compensation is possible because we set $\eta_{III} = 0$ [otherwise the scaling in Eq. (15) would have been different]. In the left panel of Fig. 4 the time evolution of the three modes with $k_{1,2,3}$ clearly shows how the initial mismatch during $N < N_I$ gets precisely reabsorbed during the phase $N_{II} < N < N_{III}$ with $\eta = 0$.

In conclusion, the formation of the plateau follows from the same mechanism that originates a scale-invariant power spectrum in the slow-roll limit when both $\epsilon \rightarrow 0$ and $|\eta| \rightarrow 0$. Modes $k^{3/2}|u_k(N)/z(N)|$ with larger k starts from larger values in the Bunch-Davies vacuum but exponentially decay for longer time before horizon crossing. In our model the presence of negative friction introduces an intermediate phase of exponential growth which however

affects all modes in the same way; the net effect is that of an exponential enhancement of the plateau value compared to the case in which the negative friction phase was absent. This is evident from the evolution of the modes shown in the left panel of Fig. 4. All in all, the mechanism that generates the plateau in our model is not fundamentally different compared to what discussed in Ref. [69] (often dubbed Wands duality, see Ref. [70]). However, the discussion presented here in terms of the evolution of individual modes gives a particularly limpid interpretation of the mechanism.

As a final remark, we reiterate the importance of solving numerically the MS equation for the computation of the power spectrum. In the right panel of Fig. 4 we show the comparison with the slow-roll approximation in Eq. (7). The slow-roll approximation captures well the overall features of the power spectrum but it misses the right modeling of the transition regions at the two edges of the plateau. These two parts of the power spectrum, as we shall discuss next, are of crucial importance for the phenomenology of PBHs.

E. Features at the edges of the plateau

Let us discuss here the role of $\delta N_{I,II,III}$ previously anticipated. First, we take $\delta N_I = \delta N_{III} = 0.50$ fixed, and consider a variation of δN_{II} with respect to the value $\delta N_{II} = 0.50$ (that is the one used in the benchmark model corresponding to the first column in Table I). We show our result in the left panel of Fig. 5. We note that δN_{II} controls the shape of the power spectrum at the left-side edge of the plateau. In particular, a sharper transition (smaller δN_{II}) results in the formation of a bumplike feature at k_{\min} ; on the contrary, a wider transition (larger δN_{II}) smooths out the bump.

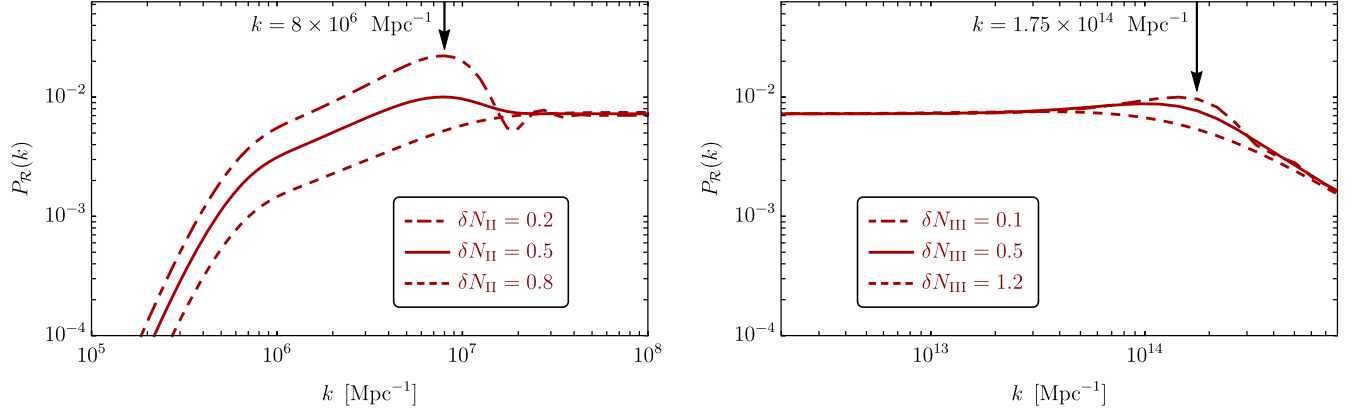


FIG. 5. Power spectrum for different choices of δN_{II} (left panel) and δN_{III} (right panel). All other parameters are fixed according to the first column in Table I. We zoom in the transition regions at the two edges of the plateau.

Second, we take $\delta N_{\text{I}} = \delta N_{\text{II}} = 0.50$ fixed, and consider a variation of δN_{III} with respect to the value $\delta N_{\text{III}} = 0.50$. We show our result in the right panel of Fig. 5. We note that δN_{III} controls the shape of the power spectrum at the right-side edge of the plateau. In particular, a sharper transition (smaller δN_{III}) results in the formation of a bump-like feature at k_{max} ; on the contrary, a wider transition (larger δN_{III}) smooths out the bump.

Let us give a closer look at the last point. As discussed in the main text, the dependence on the parameters δN_{II} and δN_{III} is an important result from a phenomenological point of view since the bumps at the left- and right-side edges of the plateau directly control the abundance of, respectively, solar- and asteroid-mass PBHs. It is, therefore, natural to ask what is the physical origin of the effect that we

described in Fig. 5. To answer this question, it is instructive to consider the dynamics of individual modes.

1. Variation of δN_{II}

We focus on the left panel of Fig. 5, and—for definiteness—consider the evolution of the mode with $k = 8 \times 10^6 \text{ Mpc}^{-1}$ (black arrow). The contribution of this mode to the power spectrum, as shown in the left panel of Fig. 5, is enhanced (suppressed) for a sharper (smoother) transition at $N = N_{\text{II}}$. We show the time evolution of this mode, both for $\delta N_{\text{II}} = 0.2$ and $\delta N_{\text{II}} = 0.8$, in the left panel of Fig. 6 (left-side of the plot, lines in red). We superimpose the time evolution of the Hubble parameter $\eta(N)$ (right-side of the plot, lines in blue). We note that this mode (as well as the other modes that form the left-side edge of the plateau)

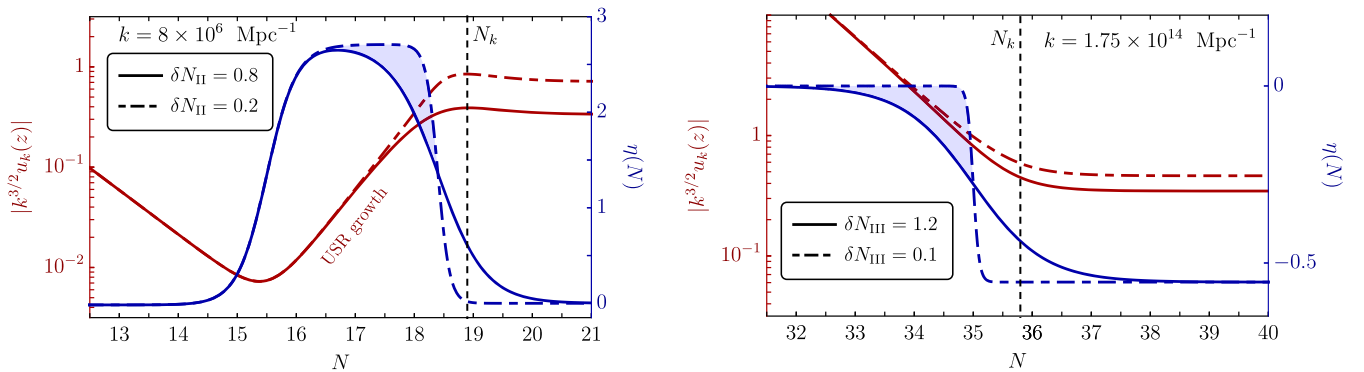


FIG. 6. Left panel. We plot the time evolution of the quantity $k^{3/2}|u_k/z|$ for $k = 8 \times 10^6 \text{ Mpc}^{-1}$ for two different values of δN_{II} (left-side y-axis, lines in red). All other free parameters are fixed to the values collected in the second column of Table I. We superimpose the time evolution of the Hubble parameter η for the same two values of δN_{II} (right-side y-axis, lines in blue). The vertical dashed line marks the horizon crossing time while (from Table I) we have $N_{\text{II}} = N_{\text{I}} + \Delta N_{\text{USR}} = 17.9$. In the region shaded in blue we have that $\eta(N)$ for $\delta N_{\text{II}} = 0.2$ is larger than $\eta(N)$ for $\delta N_{\text{II}} = 0.8$. This region highlights the difference between the two choices of δN_{II} in terms of the evolution of $\eta(N)$; the USR phase lasts for a slightly longer time if we consider smaller δN_{II} (that is a sharper transition at N_{II}). Right panel. Same as in the left panel but for $k = 1.75 \times 10^{14} \text{ Mpc}^{-1}$ and for two different values of δN_{III} (with all other free parameters kept fixed according to the second column of Table I). In the region shaded in blue we have that $\eta(N)$ for $\delta N_{\text{III}} = 0.1$ is larger than $\eta(N)$ for $\delta N_{\text{III}} = 1.2$. This region highlights the difference between the two choices of δN_{III} in terms of the evolution of $\eta(N)$; the mode experiences, before horizon crossing, a stronger exponential suppression for increasing δN_{III} , as discussed in Eq. (19).

crosses the Hubble horizon right after the end of the USR phase. As explained in the previous section, during the USR phase the mode gets exponentially enhanced. The key point is that the amount of USR depends on the sharpness of the transition at $N = N_{\text{II}}$. As evident in the left panel of Fig. 5, a very sharp transition (like in the case with $\delta N_{\text{II}} = 0.2$) gives to the same mode more time to exponentially grow. This is highlighted by the region shaded in blue in the left panel of Fig. 5. In the case with $\delta N_{\text{II}} = 0.2$ the mode has more time to grow before horizon crossing and, if compared with the evolution of the same mode but in the case of a smoother transition ($\delta N_{\text{II}} = 0.8$), it settles to a higher final value. This is the reason why the bump at the left-side edge of the plateau stands out more and more as one takes decreasing values of δN_{II} .

Before proceeding, there is one more point that is worth discussing. As evident from the left panel of Fig. 6, the bump only concerns modes that cross the horizon right after the transition time N_{II} . Plateau modes, that is modes that cross the horizon deeper during the $\eta_{\text{III}} = 0$ phase, are not sensitive on the specific value of δN_{II} . The reason is illustrated in the left panel of Fig. 7. In this figure we plot the dynamics of one of the modes that contribute to the plateau. For definiteness, we take $k = 10^8 \text{ Mpc}^{-1}$. This mode crosses the horizon at time $N_k > N_{\text{II}}$ when the value of η , for both choices $\delta N_{\text{II}} = 0.2$ and $\delta N_{\text{II}} = 0.8$, eventually settled to the value $\eta_{\text{III}} = 0$. After the end of the USR phase and before crossing the horizon at time N_k , the mode exponentially decays according to the scaling

$$k^{3/2} \left| \frac{u_k(N)}{z(N)} \right| \sim e^{-(1-\eta_{\text{III}})N}. \quad (17)$$

What happens is that if we take the case of a smooth transition the value of η_{III} is not exactly equal to zero after $N > N_{\text{II}}$ but, since the tanh function has a sizable width, it transits through a phase in which $\eta_{\text{III}} > 0$. Consequently, the mode has a slower exponential decay compared to the case of a sharp transition in which we have, from Eq. (17), the scaling e^{-N} immediately after N_{II} . Because of the symmetry of the tanh function, the slower exponential decay for $N > N_{\text{II}}$ precisely compensates the exponential growth for $N < N_{\text{II}}$ so that, independently on δN_{II} , the final value of the mode after its horizon crossing will be the same. This compensation is evident in the numerical result displayed in the left panel of Fig. 7. Importantly, this compensation works only for modes that exit the horizon at times N_k after that the transition from η_{II} to η_{III} is completed (so that they can experience while subhorizon both sides of the tanh transition at N_{II}).

2. Variation of δN_{III}

We focus on the right panel of Fig. 5, and—for definiteness—consider the evolution of the mode with $k = 1.75 \times 10^{14} \text{ Mpc}^{-1}$ (black arrow). The contribution of this

mode to the power spectrum, as shown in the right panel of Fig. 5, is enhanced (suppressed) for a sharper (smoother) transition at $N = N_{\text{III}}$. We show the time evolution of this mode, both for $\delta N_{\text{III}} = 0.1$ and $\delta N_{\text{III}} = 1.2$, in the right panel of Fig. 6 (left-side of the plot, lines in red). We superimpose the time evolution of the Hubble parameter $\eta(N)$ (right-side of the plot, lines in blue). We note that this mode (as well as the other modes that form the right-side edge of the plateau) crosses the Hubble horizon right after the transition at time N_{III} . The key point is the following. As discussed in the previous section, during its sub-Hubble evolution at times $N < N_k$, the mode evolves as

$$k^{3/2} \left| \frac{u_k(N)}{z(N)} \right| \sim e^{-(1-\eta_{\text{III}})N}, \quad (18)$$

which is the same time-dependence discussed in Eq. (15) but with η_{III} explicitly written. If we consider the case of a very smooth transition, from the $\eta(N)$ evolution displayed in right panel of Fig. 6 we see that the mode experiences a nonzero value of $\eta_{\text{III}} < 0$ already before the transition time at N_{III} while in the case of a sharper transition stays closer to $\eta_{\text{III}} = 0$ for longer time. This is highlighted by the region shaded in blue in right panel of Fig. 6. Consequently, in the case $\delta N_{\text{III}} = 1.2$ (smoother transition) the mode, before horizon crossing and for $N < N_{\text{III}}$, experiences a short phase during which it evolves as

$$k^{3/2} \left| \frac{u_k(N)}{z(N)} \right| \sim e^{-(1+|\eta_{\text{III}}|)N}, \quad (19)$$

with $\eta_{\text{III}} < 0$ nonzero and negative because of the effect of the transition region. The mode, therefore, undergoes a phase of exponential suppression that is slightly faster compared with the case of a sharper transition (for which η_{III} remains closer to zero until the actual transition at $N = N_{\text{III}}$). This is evident in right panel of Fig. 6; in the case with $\delta N_{\text{III}} = 1.2$ the mode is more suppressed and, if compared with the evolution of the same mode but in the case of a smoother transition ($\delta N_{\text{III}} = 0.1$), it settles to a lower final value. This is the reason why the bump at the right-side edge of the plateau becomes smoother and smoother as we increase the value of δN_{III} .

We note that this effect is again limited to those modes that exit the horizon right after the transition at $N = N_{\text{III}}$. Modes that exit the horizon before the transition time N_{III} (like the plateau modes) are already superhorizon, and, therefore, conserved, at time N_{III} ; modes that cross the Hubble horizon well after the transition time N_{III} (more specifically, after that η completed the transition from η_{III} to η_{IV}) experience a compensating effect that is completely analogue to the one discussed before at time N_{II} . This is shown in the right panel of Fig. 7 for the mode with $k = 2 \times 10^{14} \text{ Mpc}^{-1}$. Consider the smooth transition with $\delta N_{\text{III}} = 0.8$ (solid line). The faster exponential decrease

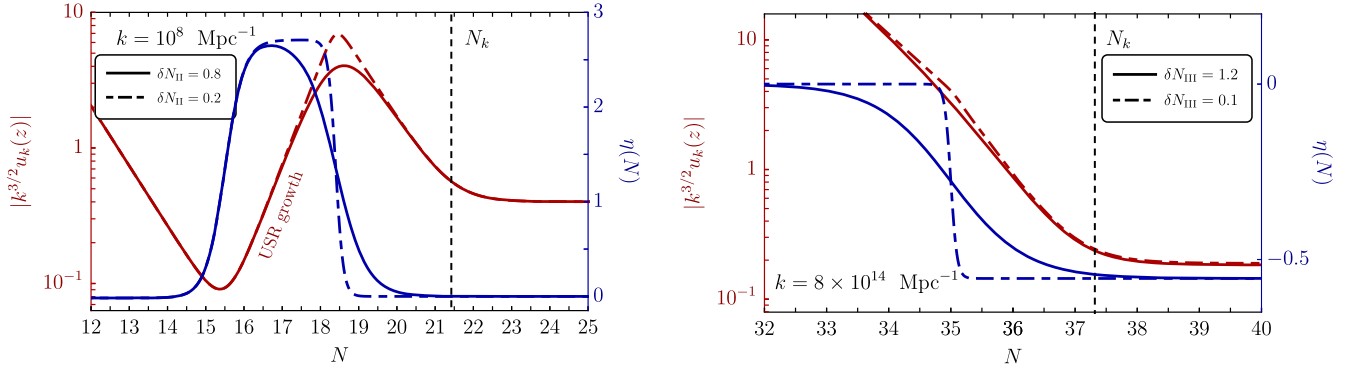


FIG. 7. Left panel. Same as in the left panel of Fig. 6 but for the time evolution of the plateau mode with $k = 10^8 \text{ Mpc}^{-1}$. Right panel. Same as in the right panel of Fig. 6 but for the time evolution of the mode with $k = 2 \times 10^{14} \text{ Mpc}^{-1}$.

right before $N = N_{\text{III}}$ is compensated by a slower exponential decrease right after the transition so that the two effects compensate at horizon crossing.

3. Variation of δN_{I}

Before concluding this section, we quickly comment about the dependence on the parameter δN_{I} which controls the sharpness of the first transition at $N = N_{\text{I}}$. The point we want to make is that changing this parameter does not alter neither the bump-like feature at the left-side edge of the plateau nor the subsequent plateau. The reason is summarized in Fig. 8. We fix $\delta N_{\text{II}} = \delta N_{\text{III}} = 0.5$ and consider two cases with $\delta N_{\text{I}} = 0.2$ and $\delta N_{\text{I}} = 1$. In the left panel, we plot the time evolution of the mode with $k = 2 \times 10^6 \text{ Mpc}^{-1}$. This mode crosses the Hubble horizon right after the end of the USR phase, and contributes to the bump-like feature at the left-edge of the plateau. Changing δN_{I} does not alter the final value of the mode because we observe, in the case of a smoother transition ($\delta N_{\text{I}} = 1$, solid lines), a compensation between a slower exponential decay right before N_{I} and the subsequent faster exponential growth right after N_{I} . In the right panel, we plot the time evolution of the plateau mode with $k = 10^8 \text{ Mpc}^{-1}$. In analogy to the previous discussion, the compensation right before and after N_{I} cancels out any difference between the final conserved value of the modes if $\delta N_{\text{I}} = 0.2$ and $\delta N_{\text{I}} = 1$ are compared. Motivated by this analysis, in the explicit realizations of our model (see Table I) we fix $\delta N_{\text{I}} = 0.5$.

In conclusion, we showed how the features at both ends of the plateau of curvature perturbations are directly controlled by δN_{II} and δN_{III} and can be simply interpreted in terms of the dynamics of the perturbation modes.

III. THE ABUNDANCE OF PBHS

In this section we review how one can compute the abundance of PBHs. Here we adopt the formalism developed in Ref. [71] that include the dependence on the equation of state, which deviates from perfect radiation around the QCD epoch when PBHs of around the solar

mass are formed. We assume that the Universe was dominated by relativistic particles at energies higher than what currently included in the standard model of particle physics, leading to a perfect radiation fluid dominating the Universe above the electroweak scale. We mention, however, that a different equation of state may be possible, implying modifications of the PBH formation [72–80] and induced SGWB [81–85] discussed in the next section.

After matter-radiation equality the dark matter fraction consisting of PBHs can be expressed as

$$\Omega_{\text{PBH}} = \int d \log M_H \left(\frac{M_{\text{eq}}}{M_H} \right)^{1/2} \beta(M_H),$$

$$f_{\text{PBH}}(M_{\text{PBH}}) = \frac{1}{\Omega_{\text{CDM}}} \frac{d\Omega_{\text{PBH}}}{d \log M_{\text{PBH}}}, \quad (20)$$

where M_H is the horizon mass at the time of horizon re-entry, $M_{\text{eq}} \simeq 3 \times 10^{17} M_{\odot}$ the horizon mass at matter-radiation equality, and Ω_{CDM} is the cold dark matter density of the Universe ($\Omega_{\text{CDM}} \simeq 0.12 h^{-2}$, with $h = 0.674$ for the Hubble parameter). The approximate relation between the horizon mass M_H and comoving wave number k_H is given by

$$M_H \simeq 17 \times \left(\frac{g_*}{10.75} \right)^{-1/6} \left(\frac{k_H}{10^6 \text{ Mpc}^{-1}} \right)^{-2} M_{\odot}, \quad (21)$$

where g_* is the number of degrees of freedom of relativistic particles with $g_* = 106.75$ deep in the radiation epoch. We include the temperature dependence of g_* following Ref. [86].¹ The mass of the resulting PBH is given by [87]

$$M_{\text{PBH}} = \mathcal{K} M_H \left[\left(\delta_{\text{L}} - \frac{1}{4\Phi} \delta_{\text{L}}^2 \right) - \delta_{\text{c}} \right]^{\gamma}. \quad (22)$$

Equation (22) automatically takes into account the nonlinear relation between curvature perturbations and the density

¹We convert the temperature dependence into a functional dependence on the horizon mass M_H by means of the relation $M_H \simeq 1.5 \times 10^5 (g_*/10.75)^{-1/2} (T/\text{MeV})^{-2} M_{\odot}$.

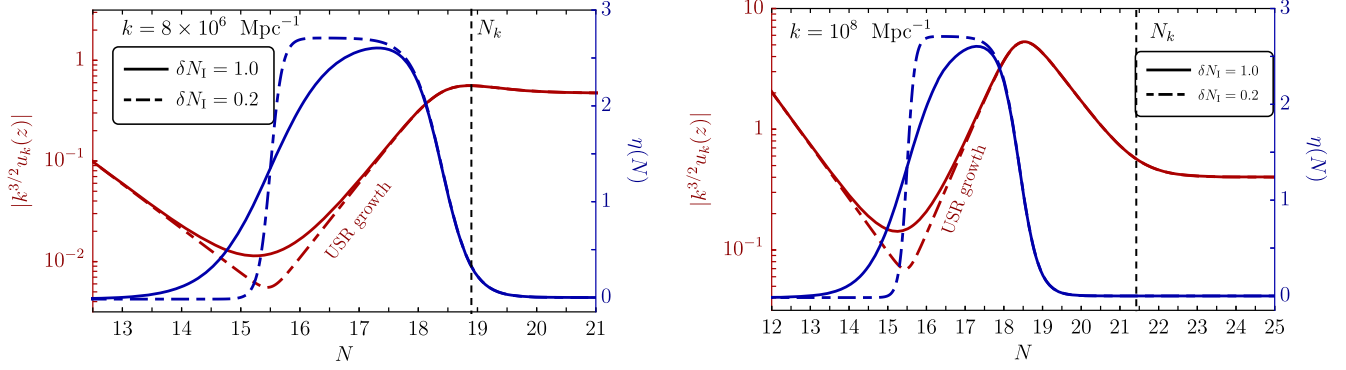


FIG. 8. Same as in Fig. 6 but now with $\delta N_{\text{II}} = \delta N_{\text{III}} = 0.5$ fixed while we vary $\delta N_{\text{I}} = 0.2$ (dot-dashed lines) and $\delta N_{\text{I}} = 1$ (solid lines). Left panel. Time evolution of the mode with $k = 8 \times 10^6 \text{ Mpc}^{-1}$ (one of the modes that contribute to the bumplike feature at the left-side edge of the plateau). Right panel. Time evolution of one of the plateau modes with $k = 10^8 \text{ Mpc}^{-1}$.

contrast field δ [87,88]. More concretely, δ_{L} represents the linear Gaussian component of the density contrast field while δ_{c} is the threshold value for gravitational collapse that refers to the full density contrast field. In full generality, $\mathcal{K}(M_{\text{H}})$, $\gamma(M_{\text{H}})$, $\Phi(M_{\text{H}})$ and $\delta_{\text{c}}(M_{\text{H}})$ are functions of the horizon mass. During the radiation epoch, \mathcal{K} typically takes a value between 3 and 5 for perturbations produced by a nearly scale-invariant spectrum [89,90], $\gamma \simeq 0.36$, $\delta_{\text{c}} \simeq 0.56$ and $\Phi = 2/3$ for a radiation fluid with equation of state parameter $\omega = p/\rho = 1/3$. In our analysis, we include the full M_{H} dependence of the above quantities following Refs. [71,91]. This is an important point since the equation of state parameter ω reduces by around 30% and the critical threshold δ_{c} decreases by around 10% during the QCD phase transition [91]. This leads to a boost in the PBH mass distribution by at least two orders of magnitude compared to a Universe in which the equation of state parameter remains constantly equal to that of radiation, $\omega = 1/3$.

The expression for β in Eq. (20) accounts for the fraction of each Hubble volume which collapses to form a PBH. Assuming threshold statistics, we have

$$\begin{aligned} \beta(M_{\text{H}}) &= \int_{\delta_{\text{c}}}^{\infty} \frac{M_{\text{PBH}}}{M_{\text{H}}} P(\delta) d\delta \\ &= \mathcal{K} \int_{\delta_{\text{L}}^{\text{min}}}^{\delta_{\text{L}}^{\text{max}}} \left(\delta_{\text{L}} - \frac{1}{4\Phi} \delta_{\text{L}}^2 - \delta_{\text{c}} \right)^{\gamma} P_{\text{G}}(\delta_{\text{L}}) d\delta_{\text{L}}, \quad (23) \end{aligned}$$

$$P_{\text{G}}(\delta_{\text{L}}) = \frac{1}{\sqrt{2\pi}\sigma(R_{\text{H}})} e^{-\delta_{\text{L}}^2/2\sigma(R_{\text{H}})^2}, \quad (24)$$

where in Eq. (23) we changed variable from the full density contrast to its linear (hence Gaussian) component. The characteristic size of perturbations is identified by the scale r_{m} where the maximum of the mass excess (or compaction function) is found [92] and it is larger than the inverse of the comoving spectral number k . For nearly scale invariant spectra, the two are related by the condition $r_{\text{m}} k \equiv \kappa \simeq 4.49$ [93]. The peak of the compaction function sets the

corresponding horizon crossing $r_{\text{m}} = 1/aH \equiv R_{\text{H}}$, where R_{H} is the comoving Hubble radius; its relation with M_{H} can be read from Eq. (21) at the time of horizon reentry $k_{\text{H}} = 1/r_{\text{m}}$. The extrema of integrations in Eq. (23) are

$$\delta_{\text{L}}^{\text{min}} = 2\Phi \left(1 - \sqrt{1 - \frac{\delta_{\text{c}}}{\Phi}} \right), \quad \delta_{\text{L}}^{\text{max}} = 2\Phi. \quad (25)$$

The variance that enters in Eq. (24) refers to the linear component of the density contrast and can be computed by integrating the power spectrum of curvature perturbations

$$\sigma^2(R_{\text{H}}) = \frac{4}{9} \Phi^2 \int_0^{\infty} (kR_{\text{H}})^4 W^2(kR_{\text{H}}) T^2(kR_{\text{H}}) P_{\mathcal{R}}(k) d \log k. \quad (26)$$

In Eq. (26) we include the Fourier transform of the top hat window function in real space $W(kR_{\text{H}})$ (used to smooth the field over a finite volume) and the linear transfer function $T(kR_{\text{H}})$ (which describes the damping of perturbations on subhorizon scales). We use²

$$\begin{aligned} W(y) &= 3 \left[\frac{\sin(y) - y \cos(y)}{y^3} \right], \\ T(y) &= 3 \left[\frac{\sin(y/\sqrt{3}) - (y/\sqrt{3}) \cos(y/\sqrt{3})}{(y/\sqrt{3})^3} \right]. \quad (27) \end{aligned}$$

Following Ref. [94], we make another change of variables from δ_{L} to M_{PBH} by inverting Eq. (22). We arrive at the final formula³

²It should be noted that the transfer function in Eq. (27) is strictly valid in a radiation-dominated phase.

³It should be noted that Ref. [32] computes the abundance of PBHs in the gaussian approximation, and includes the effect of nonlinearities by means of a final rescaling of the amplitude of the power spectrum by a factor of 2 (following the prescription given in Refs. [87,88]).

$$f_{\text{PBH}}(M_{\text{PBH}}) = \frac{1}{\Omega_{\text{CDM}}} \int_{M_H^{\text{min}}}^{\infty} \left(\frac{M_{\text{eq}}}{M_H}\right)^{1/2} \frac{e^{-\frac{8}{9\sigma(R_H)^2}[1-\sqrt{\Lambda}]^2}}{\sqrt{2\pi\sigma(R_H)\Lambda^{1/2}}} \times \left(\frac{M_{\text{PBH}}}{\gamma M_H}\right) \left(\frac{M_{\text{PBH}}}{\mathcal{K}M_H}\right)^{1/\gamma} d \log M_H, \quad (28)$$

where we conveniently defined

$$\Lambda \equiv 1 - \frac{\delta_c}{\Phi} - \frac{1}{\Phi} \left(\frac{M_{\text{PBH}}}{\mathcal{K}M_H}\right)^{1/\gamma} \quad (29)$$

in which the right-hand side can be integrated numerically to give $f(M_{\text{PBH}})$ for each value of the PBH mass. The lower limit of integration follows from the condition $\Lambda > 0$ [notice this must be the case due to the term $\sqrt{\Lambda}$ appearing in Eq. (28)]. As far as the numerical value of δ_c is concerned, it takes the value of $\delta_c = 0.56$ in a radiation-dominated universe in the case of a broad power spectrum of curvature perturbations and including the nonlinear relation between curvature perturbations and the density contrast field.⁴ It is additionally reduced and modulated when $M_H \approx M_{\odot}$ when the collapse takes place across the QCD epoch [91].

The parameters of the dynamics are chosen in such a way that the integral

$$f_{\text{PBH}} \equiv \frac{\Omega_{\text{PBH}}}{\Omega_{\text{CDM}}} = \int f_{\text{PBH}}(M_{\text{PBH}}) d \log M_{\text{PBH}} \approx 1, \quad (30)$$

which means that we get $\approx 100\%$ of DM in the form of PBHs. In Fig. 9 we show the following constraints (see Ref. [95] for a review and [96]). Envelope of evaporation constraints (see also [97–99]): EDGES [100], CMB [101], INTEGRAL [102,103], 511 keV [104], Voyager [105], EGRB [106]; microlensing constraints from the Hyper-Supreme Cam (HSC), Ref. [107]; microlensing constraints from EROS, Ref. [108]; microlensing constraints from OGLE, Ref. [109]; Icarus microlensing event, Ref. [110]; constraints from modification of the CMB spectrum due to accreting PBHs, Ref. [111]; direct constraints on PBH-PBH mergers with LIGO, Refs. [112,113] (see also [114–117]).

Recently, it was suggested that observations of Sun-like stars in dwarf galaxies may constrain the PBH abundance to be below $f_{\text{PBH}} \lesssim 0.3$ in part of the asteroidal mass window [119], i.e., for masses $M_{\text{PBH}} \lesssim 10^{-12} M_{\odot}$. Similar constraints were set in the past by studying neutron stars and white dwarfs in DM-rich environments like dwarf galaxies [120–122] (see Ref. [123] for a discussion on their validity), for which no direct observations exist to date. On the contrary, Ref. [119] focuses on main sequence stars. The newly derived bound, however, requires assuming a

⁴Reference [32] takes the value $\delta_c = 0.51$ which is the value that corresponds to the gaussian approximation, see Ref. [89].

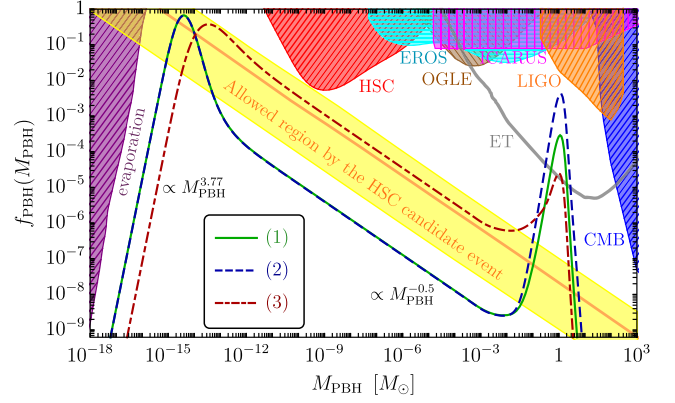


FIG. 9. Fraction of DM in the form of PBHs with mass M_{PBH} . We plot the most stringent constraints (meshed regions, cf. the SM) and the mass function resulting from three benchmark realizations of our model [labeled as (1), (2), (3), see Table I]. The yellow band corresponds to the allowed region for a PBH mass function $\propto M_{\text{PBH}}^{-0.5}$ consistent with the Subaru Hyper-Supreme-Cam (HSC) microlensing candidate event [107] (see also [118]). The gray line indicates the minimum PBH abundance required to have at least one PBH merger event per year at the Einstein Telescope (ET) experiment, see Ref. [13].

maximum allowed fraction ξ of disrupted stars that can be compatible with current observations, given the lack of precise modeling of the initial number. $\mathcal{O}(1)$ differences on ξ may completely relax this bound [119]. Therefore, we decided not to report it in Fig. 9. We conclude by pointing out that, even taking at face value the bound that follows from the assumptions made in Ref. [119], it would still be possible to tune the asteroidal mass peak in Fig. 9 in order to evade the constraint with small modifications of the parameters reported in Table I.

The resulting mass distribution is shown in Fig. 9 for three benchmark realizations of our model, all of which are chosen to reproduce all the DM in the form of PBHs ($f_{\text{PBH}} \stackrel{!}{=} 1$). The values of the parameters are collected in Table I.

The first noticeable feature of the resulting mass distribution $f_{\text{PBH}}(M_{\text{PBH}})$ is the characteristic scaling $\propto M_{\text{PBH}}^{-1/2}$ for masses produced by modes in the enhanced plateau (see Fig. 9). This is because nearly scale invariant power spectra induce the formation of PBHs of various masses with equal probability $\beta(M_H)$ [124,125], but smaller PBHs form earlier and their abundance is redshifted compared to heavier ones. This naturally induces a more prominent contribution to the DM from the light portion of the mass spectrum. Additionally, the smoothness of the transition between phases $\text{II} \rightarrow \text{III}$ and $\text{III} \rightarrow \text{IV}$, controlled by the parameters δN_{II} and δN_{III} respectively, determines the spectral features at the sides of the enhanced plateau, which are magnified in the PBH abundance due to its exponential dependence on $\mathcal{P}_{\mathcal{R}}(k)$. In particular, as already discussed in the previous section, a sharper transition

produces a more prominent oscillatory feature (see e.g., [36,126,127]), whose main peak greatly enhances the relative PBH abundance at the corresponding mass.

Focusing on the first transition, which corresponds to the formation of heavier (solar mass) PBHs, δN_{II} allows to boost f_{PBH} [on top of the softening of the QCD equation of state, whose only impact on the enhancement of the mass function can be measured by looking at case (3) in Fig. 9], to a much larger value which may potentially produce observable PBH mergers at current and future ground-based GW experiments [13,14,71,117,128–130]. On the other hand, a smaller δN_{III} would induce a peak at small masses. In the absence of a bump at asteroidal masses [i.e., case (3)], $f_{\text{PBH}}(M_{\text{PBH}})$ would be compatible with the HSC detection of a candidate lens [107] (indicated in Fig. 9 with a yellow band). On the other hand, for fixed abundance $f_{\text{PBH}} = 1$, a more pronounced peak [i.e., (1) and (2)] would decrease the amplitude of the whole tail $\propto M_{\text{PBH}}^{-1/2}$, potentially evading future HSC constraints [118].

A. On the maximum mass of PBHs in USR scenarios

We now discuss the maximum mass of PBHs that can be generated within our model. This is a delicate issue which is mostly related to the shape of the power spectrum at the left-side edge of the plateau. To make this point more clear, we start from some preliminary considerations.

In the left panel of Fig. 10 we zoom in on this part of the power spectrum. For definiteness, we consider the model dubbed (1) in Table I. Some comments are in order. First, the region shaded in magenta represents the interval of comoving wave number k such that the horizon crossing condition $k = a(N_k)H(N_k)$ falls inside the time interval $N_{\text{I}} \leq N_k \leq N_{\text{II}}$. Second, we highlight in red the part of the power spectrum that features the power-law growth $P_{\mathcal{R}}(k) \sim k^4$. We note that this part of the power spectrum lies immediately before the region shaded in magenta; this suggests that the modes that contribute to the $\sim k^4$ growth are those for which the horizon crossing condition happens right before the beginning of the USR phase. On the other hand, as already discussed at length in the previous section, the bumplike feature (highlighted with a black arrow in the left panel of Fig. 10) lies immediately after the magenta region, consistently with the fact that the modes that contribute to the bump at small k are those for which the horizon crossing condition takes place right after the USR phase. We now focus on the transition region that connects the $\sim k^4$ growth to the bump at the left-side edge of the plateau. This part of the power spectrum is formed by those modes for which horizon crossing takes place during the USR phase. In this region the slope of the power spectrum gradually decreases from $\sim k^4$ to $\sim k^{0.7}$ (regions highlighted first in blue, then in green in the left panel of Fig. 10). In order to make more explicit the interplay between the horizon crossing condition and the USR phase,

in the right panel of Fig. 10 we show the time evolution of the individual modes that contribute to the red, blue and green part of the power spectrum; we superimpose the time evolution of η , and the vertical lines mark the horizon crossing time for each mode. This plot confirms what already realized before at the level of the power spectrum; the red (blue and green) modes cross the horizon right before (during) the USR phase.

Bearing in mind the above discussion, we now come back to the issue of the maximum PBH mass. In Fig. 9, the solar-mass bump in the distribution $f_{\text{PBH}}(M_{\text{PBH}})$ is generated, at the level of the power spectrum, by the bump at the left-side edge of the plateau. Consequently, the rule of thumb is very simple; if we move the bump in $P_{\mathcal{R}}(k)$ towards smaller k we will get heavier PBHs since the solar-mass peak will shift toward increasing values of M_{PBH} . In our model, we point out two ways to accomplish this change.

- (i) The simplest option is to anticipate the beginning of the USR phase. Technically, this means taking smaller values of N_{I} . This has the net effect of a shape-invariant shift of the left-side edge of the power spectrum towards smaller k . From the left panel of Fig. 10, we see that this shift is possible until the power spectrum (more precisely, the part of it in between the red and blue region) clashes with the FIRAS bound. We illustrate our findings in Fig. 11. We consider model (1) (solid black lines in Fig. 11) and take increasingly smaller values of N_{I} . As expected, the left-side edge of the plateau shifts rigidly towards smaller k (left panel in Fig. 11). For definiteness, we focus on two specific modifications of model (1). First, consider the dashed black lines in Fig. 11 that correspond to $N_{\text{I}} = 14$. In the right panel of Fig. 11, we show the corresponding mass function $f_{\text{PBH}}(M_{\text{PBH}})$. The latter exhibits a characteristic double-peak shape. This is because we are now separating the peak due to the softer QCD equation of state (that sits at around $M_{\text{PBH}} = 1M_{\odot}$) from the peak that is due to the bump at the left-side edge of the power spectrum (that now shifted towards smaller k thus larger M_{PBH}). The height of the latter, as explained in Sec. II E 1, is controlled by δN_{II} , and the model that corresponds to the dashed black lines in Fig. 11 has $\delta N_{\text{II}} = 0.46$ thus slightly smaller than the benchmark value $\delta N_{\text{II}} = 0.5$; this is because the second peak is no longer boosted by the QCD phase transition (which, as discussed, takes place at around $M_{\text{PBH}} = 1M_{\odot}$), and we compensate this effect with a smaller δN_{II} . In this configuration the model produces a sizable abundance of PBHs with a mass function peaked at around $M_{\text{PBH}} \simeq 20M_{\odot}$. As shown in the right panel of Fig. 11, the upper bound on the abundance of these PBHs is given by LIGO data. This is an interesting point since it shows that a rigid

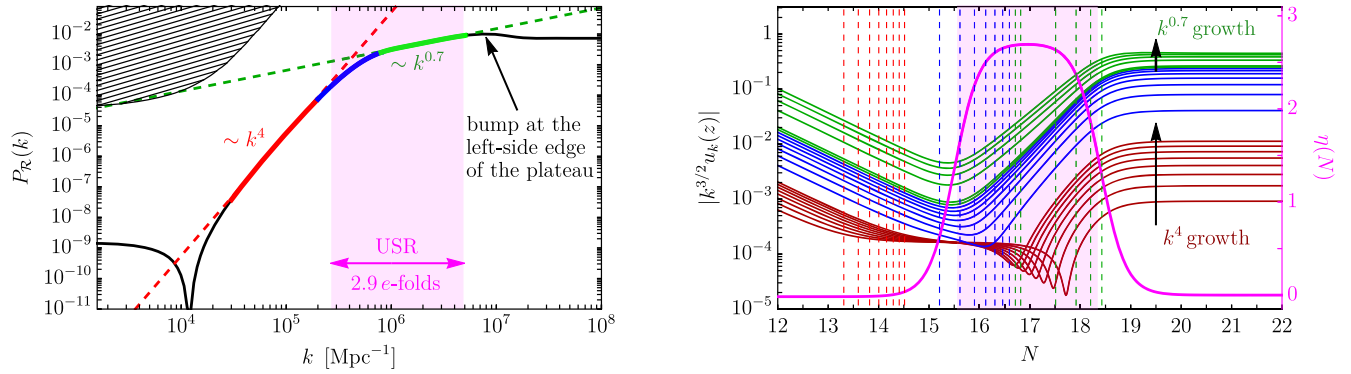


FIG. 10. Left panel: Zoom in on the left-side edge of the plateau of the power spectrum in Fig. 3. We highlight in magenta the values of k such that the horizon crossing condition $k = a(N_k)H(N_k)$ is solved for $N_I \leq N_k \leq N_{II}$. Right panel: Dynamical evolution of the perturbation modes with k in the red, blue and green part of power spectrum [cf. the use of different colors in the left panel: the red (green) part of the power spectrum corresponds to the $\sim k^4$ ($\sim k^{0.7}$) growth while the blue part lies in between]. The vertical lines mark the horizon crossing time, and make clear that for the blue and green modes we have $N_I \leq N_k \leq N_{II}$.

shift of the USR dynamics presented in the main text may generate a sufficiently abundant population of PBHs within the so-called lower mass gap, that is in the range $\approx [2.2 \div 6]M_{\odot}$ (see e.g., [131,132]), if we just take a value of N_I slightly larger than the one discussed above and in the so-called upper mass gap, that is above $\approx 50M_{\odot}$, if we just take a value of N_I slightly smaller than the one discussed above. We refer to [71] for a comprehensive discussion about the role that these PBHs may have in the gravitational-wave merger events detectable by the LVKC.

We now consider a second, much smaller value for N_I ; the dot-dashed black lines in Fig. 11 correspond to $N_I = 12.85$. From the plot of the power spectrum in the left panel of Fig. 11 we see that this value of N_I almost saturates the region allowed by the FIRAS bound. The corresponding mass distribution of PBHs is shown in the right panel of Fig. 11. The second peak is now very close to the

CMB bound, and corresponds to PBHs with mass $M_{\text{PBH}} \approx 10^2 M_{\odot}$ or larger. However, we remark that in this case the upper bound on the abundance of these PBHs is given by the CMB constraint. In the model that corresponds to the dot-dashed black lines in Fig. 11 we take $\delta N_{II} = 0.5$; if we take smaller values of δN_{II} the second peak at large PBH mass will be enhanced, in conflict with the CMB bound.

- (ii) Consider again the power spectrum in the left panel of Fig. 10. The idea is to alter the slope of the blue and green region such to connect more directly the red growth $\sim k^4$ to the bump. Thanks to our preliminary discussion, we have the right intuition about how to achieve this goal: we just need to shorten the duration of the USR phase and reach the first peak earlier. As a simple consequence, the interval of modes for which the horizon crossing condition takes place within the USR phase will be reduced. In the left panel of Fig. 12 we show the

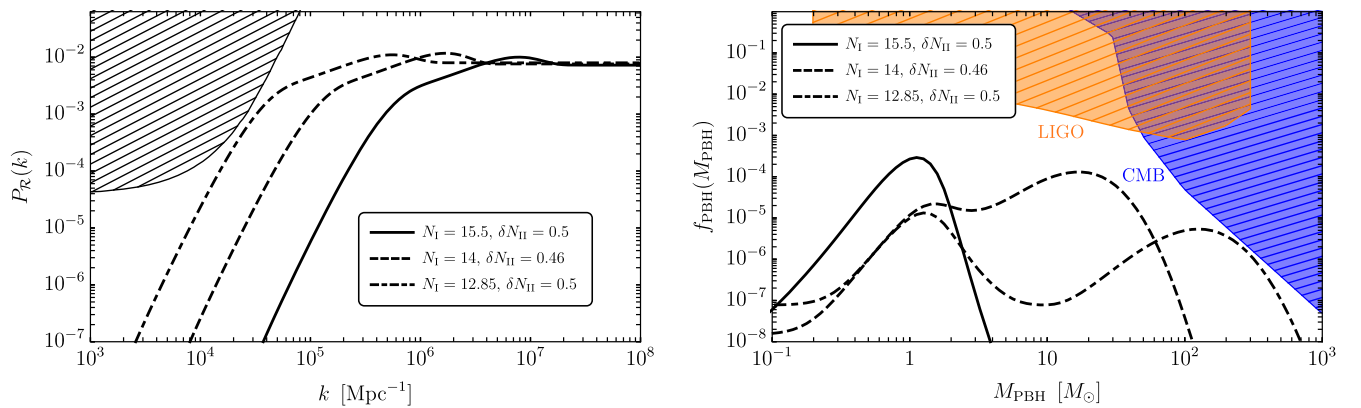


FIG. 11. Left panel: Zoom in on the left-side edge of the plateau of the power spectrum in Fig. 3; we consider two variations of model (1) that have different values of N_I and δN_{II} (cf. the plot legend for details). Right panel: Fraction of DM in the form of PBHs with mass M_{PBH} . We zoom in on the solar-mass range and show the abundance corresponding to the three models discussed in the left panel.

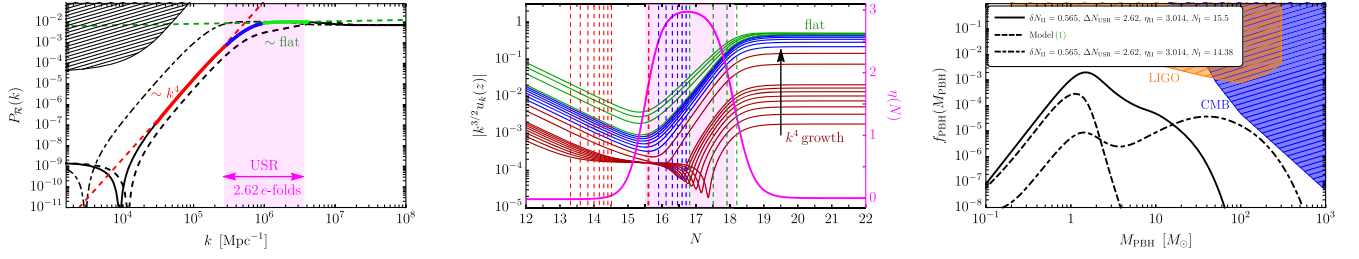


FIG. 12. Left panel: The dashed black line is the power spectrum shown in the left panel of Fig. 10; the solid black line is the power spectrum that is obtained taking $\Delta N_{\text{USR}} = 2.62$ (instead of the benchmark value $\Delta N_{\text{USR}} = 2.9$) and $\eta_{\text{II}} \simeq 3$ (instead of the benchmark value $\eta_{\text{II}} \simeq 2.7$); the dot-dashed black line is the power spectrum obtained for the same parameters given above but with an anticipated USR phase ($N_{\text{I}} = 14.38$ instead of $N_{\text{I}} = 15.5$). The red part of the power spectrum corresponds to the $\sim k^4$ growth while the green part is approximately flat; the blue part lies in between. Central panel: Dynamical evolution of the perturbation modes with k in the red, blue and green part of power spectrum discussed in the left panel. The vertical lines mark the horizon crossing time, and make clear that the for blue and green modes we have $N_{\text{I}} \leq N_k \leq N_{\text{II}}$. Right panel. The dashed black line corresponds to the PBH mass distribution in model (1). The solid black line is obtained taking a shorter URS phase with $\Delta N_{\text{USR}} = 2.6$, $\eta_{\text{II}} = 3.014$ and $\delta N_{\text{II}} = 0.565$ [but with the same $N_{\text{I}} = 15.5$ as in model (1)]. The dot-dashed black line corresponds to the same model that gives the solid black line but with an anticipated USR phase, $N_{\text{I}} = 14.38$.

power spectrum that we get if we modify model (1) by taking a shorter USR phase. We consider $\Delta N_{\text{USR}} = 2.62$ instead of the benchmark value $\Delta N_{\text{USR}} = 2.9$.

Importantly, it should be noted that, in order to maintain the same height of the plateau in the power spectrum, decreasing the value of ΔN_{USR} should be compensated by a larger value of η_{II} . This simply follows from the exponential growth in front of Eq. (13). In the left panel of Fig. 12, in fact, we are forced to consider $\eta_{\text{II}} \simeq 3$ (instead of the benchmark value $\eta_{\text{II}} \simeq 2.7$). This simple fact has a very profound implication. Since during phase I we have $\eta_{\text{I}} \simeq 0$, a Wands duality [70] is established between phase I and phase II; phases with η and $3 - \eta$ (that is, in our case, $\eta_{\text{I}} \simeq 0$ and $\eta_{\text{II}} \simeq 3 = 3 - \eta_{\text{I}}$) are dual in the sense that they give rise the same spectral slope. This means that we expect a flattening of the power spectrum during the USR phase.

The numerical analysis shown in the left panel of Fig. 12 fully confirms our intuition. For completeness, in the central panel of Fig. 12 we show the time evolution of red, blue and green modes together with their horizon crossing time (vertical lines). As expected, at the left-side edge of the plateau the power spectrum now has, as a consequence of the duality, a flat region (instead of just a bump-like feature) that is quickly connected to the $\sim k^4$ growth. From a phenomenological viewpoint, this simple modification has a far-reaching implication since it means that it will be possible to generate, at the level of the distribution $f_{\text{PBH}}(M_{\text{PBH}})$, not just a peak (as in the case of the bump-like feature) but a broader mass distribution in the LVKC detectable mass range, and extending towards heavier PBHs well within the upper mass gap. We illustrate this point in the right

panel of Fig. 12 in which we show the PBH mass distribution of the benchmark model (1) (black dashed line) compared with the one obtained for $\Delta N_{\text{USR}} = 2.62$, $\eta_{\text{II}} = 3.014$ and $\delta N_{\text{II}} = 0.565$.

Furthermore, from the left panel of Fig. 12, we also see that, in principle, we have enough room to combine (i) and (ii) and push the power spectrum towards the FIRAS bound by taking smaller values of N_{I} . Interestingly, we find that if we combine (i) and (ii) it is not possible to saturate the FIRAS bound (the minimum allowed value of N_{I} turns out to be about 14.4). The reason is that, since we now have a broader distribution in $f_{\text{PBH}}(M_{\text{PBH}})$ in the solar-mass range instead of a narrow peak, before saturating the FIRAS bound we would clash with the CMB constraint on accreting PBHs, shown in blue in Fig. 9. The black dot-dashed line in the right panel of Fig. 12 corresponds to the same model that gives the solid black line discussed before but with an anticipated USR phase ($N_{\text{I}} = 14.38$ instead of $N_{\text{I}} = 15.5$). The PBH mass distribution saturates the CMB bound even though the left-side edge of the plateau in the power spectrum is far from the FIRAS bound (cf. the dot-dashed black line in the left panel).

In conclusion, the USR dynamics studied in this paper may easily accommodate a population of solar-mass PBHs with a (potentially broad) mass distribution that extends up to the constraint provided by the modification of the CMB spectrum due to PBH accretion. A more quantitative and detailed discussion will be presented in Ref. [71].

As a final remark, we would like to stress that the above discussion shows very clearly the power of our approach. Starting from a well-defined physical question (what is the maximum mass of PBHs) we were able, in very few steps, to pinpoint a neat connection with the underlying dynamics

that made extremely clear the correct way to get to the desired answer.

IV. THE SCALAR-INDUCED GW SIGNAL

Next, we compute the second-order gravitational-wave signal sourced by scalar perturbations [15–20] (see Ref. [21] for a recent review). The current energy density of gravitational waves as function of their frequency f is given by

$$\begin{aligned} \Omega_{\text{GW}}(f) &= \frac{c_g \Omega_r}{36} \int_0^{\frac{1}{\sqrt{3}}} dt \int_{\frac{1}{\sqrt{3}}}^{\infty} ds \left[\frac{(t^2 - 1/3)(s^2 - 1/3)}{t^2 - s^2} \right]^2 \\ &\times [\mathcal{I}_c(t, s)^2 + \mathcal{I}_s(t, s)^2] P_{\mathcal{R}} \left[\frac{k\sqrt{3}}{2} (s + t) \right] \\ &\times P_{\mathcal{R}} \left[\frac{k\sqrt{3}}{2} (s - t) \right], \end{aligned} \quad (31)$$

where Ω_r is the current energy density of radiation and \mathcal{I}_c and \mathcal{I}_s are two functions that can be computed analytically (see, for instance, Refs. [133,134]). The parameter c_g defined as

$$c_g \equiv \frac{g_*(M_H)}{g_*^0} \left(\frac{g_{*S}^0}{g_{*S}(M_H)} \right)^{4/3} \quad (32)$$

accounts for the change of the effective degrees of freedom of the thermal radiation g_* and g_{*S} (where the superscript ⁰ indicates the values today) during the evolution (assuming Standard Model physics), and it is of order $c_g = 0.4$ for modes related to the formation of asteroid-mass PBHs. The frequency f is related to the comoving wave number k by the relation

$$k \simeq 6.47 \times 10^{14} \left(\frac{f}{\text{Hz}} \right) \text{Mpc}^{-1}, \quad (33)$$

so that the two sides of the flat power spectrum in Fig. 3 correspond to $f = O(0.1)$ Hz (for $k_{\text{max}} \simeq 10^{14} \text{Mpc}^{-1}$) and $f = O(10^{-9})$ Hz (for $k_{\text{min}} \simeq 10^{-9} k_{\text{max}}$). These frequencies are related to the formation of PBHs with asteroidal [135–137] and solar masses [138], respectively (see Fig. 3).

A robust prediction of this scenario, as highlighted in Ref. [32], is the generation of a nearly scale invariant SGWB (shown in Fig. 13) crossing both PTA experiments and LISA. Due the quadratic dependence of the SGWB amplitude to the spectrum amplitude, one finds much milder features mirroring the large enhancements observed in the PBH mass distribution. However, it is interesting to notice that δN_{II} would potentially modify the spectral tilt within the PTA frequency range, ranging from flat to slightly red in scenarios (3) and (1), respectively. In all cases, such spectrum has a frequency dependence in the

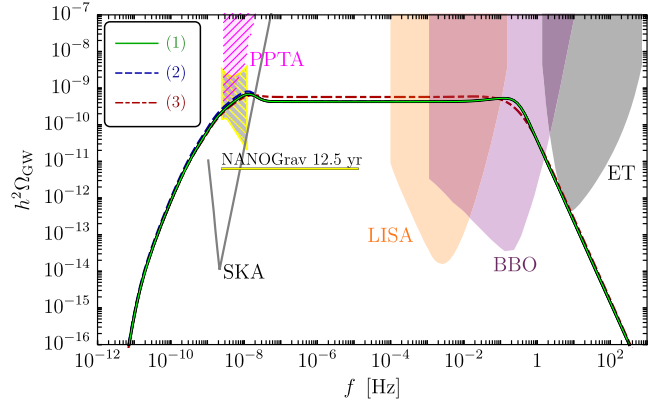


FIG. 13. Fraction of the energy density in GWs relative to the critical energy density of the Universe as function of the frequency. We show the power-law integrated sensitivity curves [140] of future ground- and space-based GW experiments (as derived in Appendix C of Ref. [141]) as well as previous Parkes Pulsar Timing Array (PPTA) constraint [142], NANOGrav putative band [25] and SKA projected sensitivity [143]. We plot the signals predicted by our model in the three realizations proposed in Table I.

PTA range which is different from the one emitted by massive BH binaries (e.g., [139]).

Before proceeding, let us comment on a number of approximations that we have done in the computation of the scalar-induced GW signal. First, we remark that Eq. (31) and the value $c_g = 0.4$ are strictly valid only during the radiation epoch with $g_* = O(100)$. In principle, one should modify Eq. (31) to include the effect of the QCD quark-hadron phase transition (along the lines of what is done in Ref. [144]). This is particularly relevant for the comparison with experimental data in the low-frequency region of PTA and NANOGrav. Future confirmation of the NANOGrav signal with additional spectral information will make this computation extremely relevant for an appropriate comparison between theoretical predictions and data. We leave this analysis for future work. Second, as done throughout this work, we neglect possible primordial non-Gaussian corrections in the computation of the scalar-induced GW signal. We refer to Refs. [145–148] for a discussion about the impact of these effects.

V. THE RECONSTRUCTED POTENTIAL

From $\eta(N)$ and $\epsilon(N)$, that capture the inflationary dynamics and connects it to the various late time observable, we can reconstruct the scalar potential $V(\phi)$. This is the final aim of the reverse engineer approach and one of the main results of our paper.

A. From dynamics to the inflationary potential

Once the Hubble parameters are known, one can compute the inflationary potential by means of

$$V(N) = V(N_{\text{ref}}) \exp \left\{ -2 \int_{N_{\text{ref}}}^N dN' \left[\frac{\epsilon(3-\eta)}{3-\epsilon} \right] \right\},$$

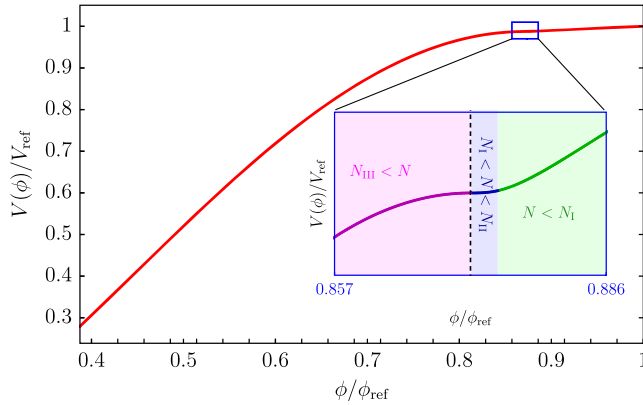
$$\phi(N) = \phi(N_{\text{ref}}) \pm \int_{N_{\text{ref}}}^N dN' \sqrt{2\epsilon}, \quad (34)$$

where in the second equation we consider the minus sign having in mind a large-field model in which the field value decreases as inflation proceeds. Combining $V(N)$ and $\phi(N)$, we reconstruct the profile $V(\phi)$ of the inflationary potential in field space [68]. We will discuss further details of the reconstruction procedure and the interpretation of the potential remainder of this section. We mention here that Eq. (34) shows the convenience of modeling the inflationary dynamics directly at the level of η instead of $V(\phi)$. This is because the Hubble parameters enters at the exponent of the definition of $V(N)$, and thus allow for a much finer control on power spectral features when performing the reverse engineering procedure.

Using the reconstructed potential $V(\phi)$, one can also solve the inflaton equation of motion

$$\frac{d^2\phi}{dN^2} + \left[3 - \frac{1}{2} \left(\frac{d\phi}{dN} \right)^2 \right] \left[\frac{d\phi}{dN} + \frac{d \log V(\phi)}{d\phi} \right] = 0, \quad (35)$$

and, in turn, compute the time evolution of the Hubble parameters in Eq. (1) and the Hubble rate by means of the relations



$$\epsilon = \frac{1}{2} \left(\frac{d\phi}{dN} \right)^2, \quad \eta = 3 - \frac{V'(\phi)[-6 + (d\phi/dN)^2]}{2V(\phi)(d\phi/dN)},$$

$$(3-\epsilon)H^2 = V(\phi). \quad (36)$$

As far as the Hubble parameters are concerned, these equations are nothing but a rewriting of Eq. (1) in terms of the classical field dynamics while the last equation is the Friedmann equation. These equations are valid under the assumption that the energy density of the inflating Universe is given entirely by the scalar field ϕ . As a consistency check, we correctly find the same functional dependence illustrated in Fig. 2 (but now obtained as an output instead of an input).

The presence of an USR phase is typically associated with an (approximate) stationary inflection point in the potential of the inflaton. This is what we obtain by following the reconstruction procedure. In the left panel of Fig. 14 we show the reconstructed potential that corresponds to model (1) (cf. Table I). In the right panel of the same figure, we plot the inflationary trajectory in the phase space of the inflaton field. At first sight, the reconstructed potential is characterized by a flattish region at large field values (where we fit the CMB observables) followed by a steeper decrease that ends inflation. However, a closer look (see the inset plot in the left panel of Fig. 14) reveals the presence of a transition region which plays a crucial role for the manifestation of the USR dynamics. During the time interval $N_I < N < N_{II}$ the field breaks its slow rolling and spends the next e -fold time interval $N_{II} < N < N_{III}$ almost stuck in field space

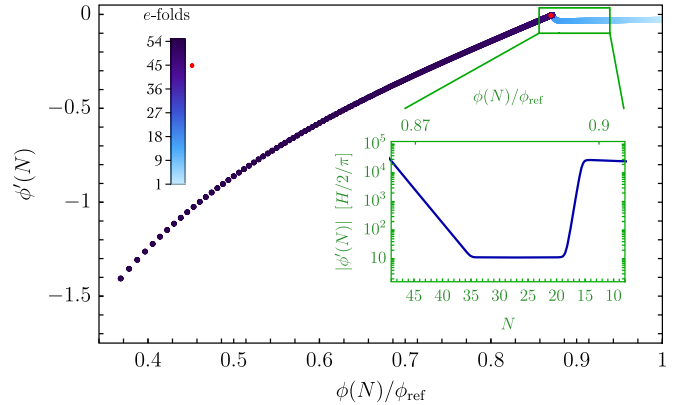


FIG. 14. Left panel: Reconstructed potential for the model in the second column of Table I. In the inset plot, we zoom in the transition region, and we indicate with different colors the various stages of the classical inflaton dynamics. It should be noted that during the time interval $N_{II} < N < N_{III}$ (shown as dashed vertical line) the inflaton field has almost zero velocity and it remains approximately stuck in field space (with this part of the dynamics that lasts for about $\Delta N_{\text{plateau}} \simeq 18$ e -folds) before entering the last stage that ends inflation. Right panel: Phase-space classical dynamics of the inflaton field. Different gradations of blue correspond, according to the inset legend, to increasing e -fold time N starting from $N_{\text{ref}} = 0$ (lighter) to the end of inflation $N_{IV} = 55$ (darker). The red dot corresponds to $N = 45$. On the y -axis, the field has units of reduced Planck mass and we use the notation $\phi' = d\phi/dN$. In the inset plot, we plot the modulus of the velocity in units of $H/2\pi$ as function of N (with the corresponding field values on the top x -axis), and we focus on the USR phase and the subsequent phase during which $\eta_{III} = 0$. We note that, in units of $H/2\pi$, we have $|\phi'(N)| \gg 1$ during the whole dynamics with $|\phi'(N)| = O(10)$ during the phase with $\eta_{III} = 0$.

retaining just the right amount of inertia to cross the transition region and ends inflation.

It is important to stress that the part of the dynamics that corresponds to the formation of the plateau in the power spectrum, that is the e -fold time interval $N_{\text{II}} < N < N_{\text{III}}$ (cf. the schematic evolution in Fig. 2), is hidden within a tiny region in field space (to the point of being just a vertical line in the left panel of Fig. 14). The reverse engineering approach proposed in this paper, therefore, seems to be the right language to capture and describe such a finely tuned part of the inflationary dynamics.

B. Interpretation within single-field models

Consider for instance the following potential

$$V_n(\phi) = \frac{V_0}{(n-2)^2} \left\{ [-4c_4(n-1) + n(n-1+c_3)] \times \left(\frac{\phi}{\phi_0}\right)^2 + n(1-c_3) \left(\frac{\phi}{\phi_0}\right)^{2n-2} - 4(n-1)(1-c_4) \left(\frac{\phi}{\phi_0}\right)^n \right\}. \quad (37)$$

This potential (of the type $\phi^2 + \phi^3 + \phi^4$ for $n=3$ and $\phi^2 + \phi^4 + \phi^6$ for $n=4$), by construction, features at $\phi = \phi_0$ a stationary inflection point (i.e., $V'(\phi_0) = V''(\phi_0) = 0$) if $c_{3,4} = 0$. Values $c_{3,4} \neq 0$ parametrize deviations from this exact configuration (approximate stationary inflection point). By construction, $V_0 \equiv V_n(\phi_0)$.

For illustration, we compare in the left panel of Fig. 15 the functional form given by $V_4(\phi)$ with the reconstructed potential. We take $\phi_0 = \phi_{\text{II}} \equiv \phi(N_{\text{II}})$ (that is the field value

at which for the reconstructed potential we have $V'(\phi_0) \approx V''(\phi_0) \approx 0$). The comparison (see the caption of Fig. 15 for details) suggests that the potential with an approximate stationary inflection point is not the best-suited candidate to reproduce our numerical result.

For this reason, we explore an alternative route. We note that during the first phase of the dynamics the potential can be computed analytically solving the system in Eq. (34). We find

$$V_{\text{SR}}(\phi) = V_{\text{ref}} \left[\frac{6 - 2\epsilon_1 - 2\eta_1 \sqrt{2\epsilon_1} (\phi - \phi_{\text{ref}}) - \eta_1^2 (\phi - \phi_{\text{ref}})^2}{2(3 - \epsilon_1)} \right]^{1 - \frac{3}{\eta_1}}, \quad (38)$$

with the subscript SR that indicates that this potential describes the initial slow-roll dynamics. In this analytical derivation, we assumed the linear term in ϵ appearing in Eq. (1) is negligible, which is justified during the initial slow-roll phase. In addition, we consider the potential (with the subscript BSR that generically indicates that this potential describes the dynamics beyond the initial slow-roll phase)

$$V_{\text{BSR}}(\phi) = \frac{3V_0 - 4\lambda(2 + c_4)}{3} + 4\lambda \left(\frac{\phi}{\phi_0}\right)^2 \times \left[1 + c_4 \left(\frac{\phi}{\phi_0}\right)^2 - \frac{(1 + 2c_4)}{3} \left(\frac{\phi}{\phi_0}\right)^4 \right], \quad (39)$$

with, by construction, $V_{\text{BSR}}(\phi_0) = V_0$ and $V'_{\text{BSR}}(\phi_0) = 0$.

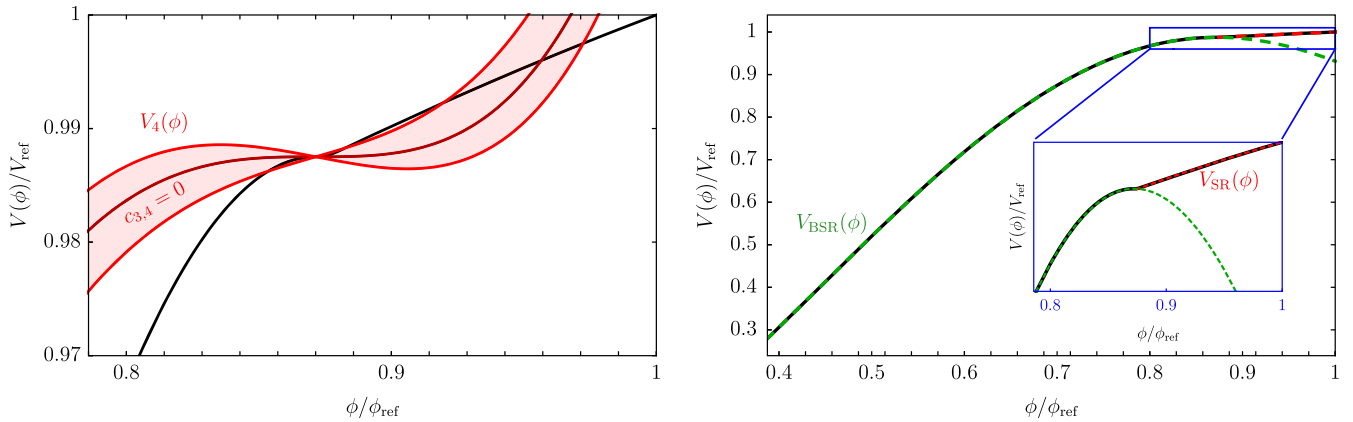


FIG. 15. Left panel: We compare the reconstructed potential (solid black line) with a benchmark potential featuring an approximate stationary inflection point (anchored to the field value at which $V'(\phi_0) = V''(\phi_0) = 0$ with ϕ_0 chosen to be the field value at $N = N_{\text{II}}$). The latter is given by Eq. (37) with $n=4$ and $c_{3,4} = 0$ (solid red line). The region shaded in red is obtained for nonzero $c_{3,4}$ at the percent level. Right panel: We model the reconstructed potential (solid black line) with a combination of the potential in Eq. (38) (dashed red, label $V_{\text{SR}}(\phi)$) and Eq. (39) (dashed green, label $V_{\text{BSR}}(\phi)$). For the potential $V_{\text{SR}}(\phi)$ we use the values of the parameters given in Table I (since this is the actual analytical solution of the system in Eq. (34) during the initial slow-roll phase). In the case of $V_{\text{BSR}}(\phi)$, we take $V_0 \simeq 0.988$, $\lambda \simeq 0.714$, $c_4 \simeq -0.748$ and $\phi_0 \simeq 3.054$; we extract these values from a fit of the reconstructed potential considering the region $\phi < \phi_1 = \phi(N_1)$. In the reconstructed potential we take $\phi_{\text{ref}} = 3.5$.

C. Interpretation within multifield models

The reconstructed potential suggests that $V(\phi)$ could be obtained by a combination of Eqs. (38) and (39). This is shown in the right panel of Fig. 15. In the following, we will make a few comments to motivate this intuition within multifield models of inflation. We focus for simplicity on two-field models.

1. Two-field models: Classical dynamics

Consider a double inflation model with two scalar fields $\phi_{1,2}$ and potential $V = V(\phi_1, \phi_2)$. To fix ideas, we can think about the full potential V as the sum of two independent contributions, $V = V(\phi_1) + V(\phi_2)$ (even though the following discussion will be valid for a generic V). The classical equations of motion and the Friedmann equation are (we indicate with $\dot{}$ derivative with respect to the cosmic time t)

$$\begin{aligned} \ddot{\phi}_1 + 3H\dot{\phi}_1 + V_{\phi_1} &= 0, & \ddot{\phi}_2 + 3H\dot{\phi}_2 + V_{\phi_2} &= 0, \\ H^2 &= \frac{1}{3} \left(\frac{1}{2}\dot{\phi}_1^2 + \frac{1}{2}\dot{\phi}_2^2 + V \right), \end{aligned} \quad (40)$$

where we use the short-hand notation $V_x \equiv \partial V / \partial x$. Inflation proceeds along some trajectory σ in field space that we describe by means of the velocity field

$$\dot{\sigma} = \dot{\phi}_1 \cos \theta + \dot{\phi}_2 \sin \theta. \quad (41)$$

For a schematic representation of the inflationary trajectory and its velocity in the multi-field space, see Fig. 16. Since there is no velocity in the transverse direction, we also have $\dot{\phi}_1 \sin \theta = \dot{\phi}_2 \cos \theta$; consequently, we find $\dot{\sigma}^2 = \dot{\phi}_1^2 + \dot{\phi}_2^2$. It should be noted that, in general, the angle θ depends on time. If we combine the time derivative of Eq. (41) with the equations of motion for $\phi_{1,2}$ we find $\ddot{\sigma} + 3H\dot{\sigma} + V_\sigma = 0$, where $V_\sigma = V_{\phi_1} \cos \theta + V_{\phi_2} \sin \theta$. All in all, instead of the system in Eq. (40), it is possible to describe the dynamics from the point of view of the effective inflationary trajectory by means of the equations

$$H^2 = \frac{1}{3} \left(\frac{1}{2}\dot{\sigma}^2 + V \right), \quad \ddot{\sigma} + 3H\dot{\sigma} + V_\sigma = 0. \quad (42)$$

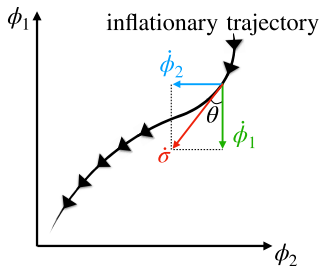


FIG. 16. Schematic representation of the inflationary trajectory in field space.

Given the above expression for H , we now compute the Hubble parameters in Eq. (1). A simple computation shows that (using the number of e -folds as time variable)

$$\epsilon = \frac{1}{2} \left(\frac{d\sigma}{dN} \right)^2, \quad \eta = 3 + \frac{V_\sigma [6 - (d\sigma/dN)^2]}{2V(d\sigma/dN)}. \quad (43)$$

We rewrite these equations in the form

$$d\sigma = \pm \sqrt{2\epsilon} dN, \quad \frac{dV}{V} = \left[\frac{2\epsilon(\eta - 3)}{3 - \epsilon} \right] dN. \quad (44)$$

We note that these equations retain precisely the same form compared to Eq. (34). This means that the reverse engineering approach can be equally well applied to the case in which ϕ represents the effective inflationary trajectory σ of a multifield model. In the latter case, the reconstructed potential will be the potential felt by the effective inflationary trajectory. From this perspective, it is therefore plausible that the reconstructed potential features, as function of the effective trajectory, a nontrivial profile like the one found in Fig. 15 since inflation could be mostly driven in the first stage by one of the two fields [with potential, say, $V(\phi_1)$] and during a subsequent phase by the other [with potential, say, $V(\phi_2)$].

2. Two-field models: Perturbations

The previous discussion was purely classical. However, the reverse engineering approach requires the solution of the MS equation on the reconstructed potential. What is the analogue of this part of the analysis in the case of a two-field model? To answer this question, we introduce adiabatic ($\delta\sigma$) and entropy (δs) perturbations

$$\begin{aligned} \delta\sigma &= \delta\phi_1 \cos \theta + \delta\phi_2 \sin \theta, \\ \delta s &= \delta\phi_2 \cos \theta - \delta\phi_1 \sin \theta. \end{aligned} \quad (45)$$

The total comoving curvature perturbation \mathcal{R} takes the form [149]

$$\begin{aligned} \mathcal{R} &= \psi - HV = \psi + \frac{H}{(\dot{\phi}_1^2 + \dot{\phi}_2^2)} (\dot{\phi}_1 \delta\phi_1 + \dot{\phi}_2 \delta\phi_2) \\ &= \psi + \frac{H}{\dot{\sigma}^2} (\dot{\sigma} \cos \theta \delta\phi_1 + \dot{\sigma} \sin \theta \delta\phi_2) = \psi + \frac{H}{\dot{\sigma}} \delta\sigma, \end{aligned} \quad (46)$$

where ψ is the gauge-dependent curvature perturbation and V the total velocity perturbation [149]. We note that the expression for \mathcal{R} , written in terms of the field σ , is identical to that for a single field. We now assume the absence of entropy perturbations, $\delta s = 0$. From Eq. (45), it follows that $\delta\phi_2 \cos \theta = \delta\phi_1 \sin \theta$; combined with the classical relation $\dot{\phi}_1 \sin \theta = \dot{\phi}_2 \cos \theta$, it gives the condition $\delta\phi_1 / \dot{\phi}_1 = \delta\phi_2 / \dot{\phi}_2$. Under this assumption, it is possible to show that the equation governing the evolution of adiabatic perturbation is the same as that in the single field inflation [149]; in Fourier space, it reads

$$u_k'' + \left(k^2 - \frac{z''}{z}\right)u_k = 0, \quad (47)$$

where $u_k = -zR_k$, $z = a\dot{\sigma}/H$ and ' indicates derivative with respect to the conformal time. Using the number of e -folds as time variable, the previous equation takes precisely the same form of the MS equation in Eq. (8) but with the Hubble parameters ϵ and η given in terms of the effective inflationary trajectory as in Eq. (43). The power spectrum of adiabatic perturbation is again given by Eq. (10).

The conclusion of this brief discussion is the following. The reverse engineering approach implemented in the context of single-field inflationary models could be also applied in the case of two-field models under the assumption of negligible entropy perturbations. The key difference is that the role of the inflaton field ϕ is played by the effective inflationary trajectory σ . In such a case, the reconstructed potential corresponds to the potential along the trajectory σ ; the latter could be the result of a nontrivial combination of different potentials along different directions in field space as possibly suggested by our numerical result shown in Fig. 15.

It should be noted that, in general, entropy perturbations are nonzero and act as an additional source term in the equation of motion for the adiabatic field perturbation [149]. However, there are cases in which their dynamics decouples. The equation of motion of δs is indeed characterized by an effective mass squared term that, if $\gg H^2$, effectively decouples entropy from adiabatic perturbations [149] (see also Ref. [150] for a recent discussion of PBH formation in the context of multifield inflation with non-minimal couplings). Moreover, if the trajectory in field space is not strongly curved (that is, more specifically, if $\dot{\theta}^2 \ll H^2$) entropy perturbations also decouple [149].

Needless to say, the above discussion about inflationary models that fit our numerical results is anything but comprehensive. On the one hand, keeping the discussion at this level suits the spirit of this paper since the main point of our analysis is precisely that of moving the attention from the details of the inflationary potential to the underlying dynamics. On the other one, finding concrete and motivated models that reproduce the reconstructed potential plays an important role in our understanding of PBH formation. In this sense, our results could stimulate new research in this direction since we are not aware of consistent inflationary models that generate a plateau in the power spectrum like the one found in our analysis.

VI. CONCLUSIONS AND OUTLOOK

In this paper, we have discussed the details of the reverse engineering technique presented in Ref. [31] for studying the consequences of an USR phase during the inflationary dynamics. This approach models the time evolution of the Hubble parameter η , Eq. (2), and gives as output the power spectrum of curvature perturbation, Fig. 3. Our approach

makes intuitively clear all features of the power spectrum, and offers a neat connection with a number of key observables related to PBH physics.

For the first time, we have shown that an USR dynamics consistent with CMB data may generate a raised plateau in the power spectrum of curvature perturbation that can provide a link between three observables; DM made of asteroid-mass PBHs (Fig. 9), a detectable stochastic GW signal (Fig. 13) and an observable fraction of solar-mass mergers ascribable to PBHs (Fig. 9). We expect our results to foster new research on consistent inflationary models able to generate a raised plateau in the power spectrum, like the one found in our analysis, giving rise to various interconnected observational signatures of the physics of the early Universe. In this respect, it will be important to extend the discussion drafted in Sec. V with the goal of finding motivated scalar field potentials that give the dynamics envisaged by our reverse engineering approach.

In general, USR dynamics is expected to produce a dip in the curvature spectrum, as the one observed in Fig. 3 around $\text{few} \times 10^3 \text{ Mpc}^{-1}$. This dip may be a complementary probe of this scenario leaving detectable imprints in CMB μ -space distortions [151] or 21 cm signals [152].

Furthermore, the population of PBHs generated within our model may give rise to detectable events both in the sub-solar range, which is a smoking-gun signature of primordial origin [153], and in the purported lower mass gap, predicting a dearth of events within $\approx [2.2 \div 6]M_\odot$ (see e.g., [131,132]). In particular, it may help explaining some of the special events already observed, such as GW190814 [71] (see also [128]). Within our framework, it is also possible to explain events in the upper mass gap, potentially produced by stellar evolution above $\approx 50M_\odot$ [154–158], such as GW190521 [159,160]; to this end, it is crucial to understand how to properly shape the left-side edge of the plateau in the power spectrum such as to populate the higher-mass region without violating the FIRAS bound, see Ref. [71] for more details. PBH mergers associated to the bulk of the PBH mass distribution in the asteroidal mass range would give rise to GWs at ultra-high frequencies, which may be potentially observed at GW detectors (see Ref. [161] and references therein).

ACKNOWLEDGMENTS

We thank G. Ballesteros, V. De Luca, I. Musco, P. Pani, A. Riotto, M. Taoso, and H. Veermäe for discussions. G. F. acknowledges financial support provided under the European Union's H2020 ERC, Starting Grant Agreement No. DarkGRA–757480 and under the MIUR PRIN programme, and support from the Amaldi Research Center funded by the MIUR program “Dipartimento di Eccellenza” (CUP: B81I18001170001). This work was supported by the EU Horizon 2020 Research and Innovation Programme under the Marie Skłodowska-Curie Grant Agreement No. 101007855.

- [1] Y. Akrami *et al.* (Planck Collaboration), *Astron. Astrophys.* **641**, A10 (2020).
- [2] P. A. R. Ade *et al.* (BICEP, Keck Collaborations), *Phys. Rev. Lett.* **127**, 151301 (2021).
- [3] R. Kallosh and A. Linde, *J. Cosmol. Astropart. Phys.* **12** (2021) 008.
- [4] Y. B. Zel'dovich and I. D. Novikov, *Sov. Astron. AJ* (Engl. Transl.) **10**, 602 (1967).
- [5] S. W. Hawking, *Nature (London)* **248**, 30 (1974).
- [6] G. F. Chapline, *Nature (London)* **253**, 251 (1975).
- [7] B. J. Carr, *Astrophys. J.* **201**, 1 (1975).
- [8] P. Ivanov, P. Naselsky, and I. Novikov, *Phys. Rev. D* **50**, 7173 (1994).
- [9] J. Garcia-Bellido, A. D. Linde, and D. Wands, *Phys. Rev. D* **54**, 6040 (1996).
- [10] P. Ivanov, *Phys. Rev. D* **57**, 7145 (1998).
- [11] S. Blinnikov, A. Dolgov, N. K. Porayko, and K. Postnov, *J. Cosmol. Astropart. Phys.* **11** (2016) 036.
- [12] H. Motohashi and W. Hu, *Phys. Rev. D* **96**, 063503 (2017).
- [13] V. De Luca, G. Franciolini, P. Pani, and A. Riotto, *J. Cosmol. Astropart. Phys.* **11** (2021) 039.
- [14] O. Pujolas, V. Vaskonen, and H. Veermäe, *Phys. Rev. D* **104**, 083521 (2021).
- [15] K. Tomita, *Prog. Theor. Phys.* **54**, 730 (1975).
- [16] S. Matarrese, O. Pantano, and D. Saez, *Phys. Rev. Lett.* **72**, 320 (1994).
- [17] V. Acquaviva, N. Bartolo, S. Matarrese, and A. Riotto, *Nucl. Phys.* **B667**, 119 (2003).
- [18] S. Mollerach, D. Harari, and S. Matarrese, *Phys. Rev. D* **69**, 063002 (2004).
- [19] K. N. Ananda, C. Clarkson, and D. Wands, *Phys. Rev. D* **75**, 123518 (2007).
- [20] D. Baumann, P. J. Steinhardt, K. Takahashi, and K. Ichiki, *Phys. Rev. D* **76**, 084019 (2007).
- [21] G. Domènech, *Universe* **7**, 398 (2021).
- [22] P. Auclair *et al.* (LISA Cosmology Working Group), [arXiv:2204.05434](https://arxiv.org/abs/2204.05434).
- [23] K. A. Kuns, H. Yu, Y. Chen, and R. X. Adhikari, *Phys. Rev. D* **102**, 043001 (2020).
- [24] A. Sesana *et al.*, *Exp. Astron.* **51**, 1333 (2021).
- [25] Z. Arzoumanian *et al.* (NANOGrav Collaboration), *Astrophys. J. Lett.* **905**, L34 (2020).
- [26] B. Goncharov *et al.*, *Astrophys. J. Lett.* **917**, L19 (2021).
- [27] S. Chen *et al.*, *Mon. Not. R. Astron. Soc.* **508**, 4970 (2021).
- [28] J. Antoniadis *et al.*, *Mon. Not. R. Astron. Soc.* **510**, 4873 (2022).
- [29] D. J. Fixsen, E. S. Cheng, J. M. Gales, J. C. Mather, R. A. Shafer, and E. L. Wright, *Astrophys. J.* **473**, 576 (1996).
- [30] S. Bird, H. V. Peiris, M. Viel, and L. Verde, *Mon. Not. R. Astron. Soc.* **413**, 1717 (2011).
- [31] G. Franciolini and A. Urbano, [arXiv:2207.10056](https://arxiv.org/abs/2207.10056).
- [32] V. De Luca, G. Franciolini, and A. Riotto, *Phys. Rev. Lett.* **126**, 041303 (2021).
- [33] H. V. Ragavendra, P. Saha, L. Sriramkumar, and J. Silk, *Phys. Rev. D* **103**, 083510 (2021).
- [34] G. Tasinato, *Phys. Rev. D* **103**, 023535 (2021).
- [35] K.-W. Ng and Y.-P. Wu, *J. High Energy Phys.* **11** (2021) 076.
- [36] A. Karam, N. Koivunen, E. Tomberg, V. Vaskonen, and H. Veermäe, [arXiv:2205.13540](https://arxiv.org/abs/2205.13540).
- [37] K. Inomata, M. Kawasaki, K. Mukaida, Y. Tada, and T. T. Yanagida, *Phys. Rev. D* **95**, 123510 (2017).
- [38] J. Garcia-Bellido and E. Ruiz Morales, *Phys. Dark Universe* **18**, 47 (2017).
- [39] G. Ballesteros and M. Taoso, *Phys. Rev. D* **97**, 023501 (2018).
- [40] M. P. Hertzberg and M. Yamada, *Phys. Rev. D* **97**, 083509 (2018).
- [41] K. Kannike, L. Marzola, M. Raidal, and H. Veermäe, *J. Cosmol. Astropart. Phys.* **09** (2017) 020.
- [42] I. Dalianis, A. Kehagias, and G. Tringas, *J. Cosmol. Astropart. Phys.* **01** (2019) 037.
- [43] K. Inomata, M. Kawasaki, K. Mukaida, and T. T. Yanagida, *Phys. Rev. D* **97**, 043514 (2018).
- [44] D. Y. Cheong, S. M. Lee, and S. C. Park, *J. Cosmol. Astropart. Phys.* **01** (2021) 032.
- [45] N. Bhaumik and R. K. Jain, *J. Cosmol. Astropart. Phys.* **01** (2020) 037.
- [46] N. Bhaumik and R. K. Jain, *Phys. Rev. D* **104**, 023531 (2021).
- [47] G. Ballesteros, J. Rey, M. Taoso, and A. Urbano, *J. Cosmol. Astropart. Phys.* **07** (2020) 025.
- [48] L. Iacconi, H. Assadullahi, M. Fasiello, and D. Wands, *J. Cosmol. Astropart. Phys.* **06** (2022) 007.
- [49] S. Kawai and J. Kim, *Phys. Rev. D* **104**, 083545 (2021).
- [50] J. E. Lidsey, A. R. Liddle, E. W. Kolb, E. J. Copeland, T. Barreiro, and M. Abney, *Rev. Mod. Phys.* **69**, 373 (1997).
- [51] M. Sasaki, *Prog. Theor. Phys.* **76**, 1036 (1986).
- [52] V. F. Mukhanov, *Sov. Phys. JETP* **67**, 1297 (1988).
- [53] G. Ballesteros, J. Rey, M. Taoso, and A. Urbano, *J. Cosmol. Astropart. Phys.* **08** (2020) 043.
- [54] C. Pattison, V. Vennin, H. Assadullahi, and D. Wands, *J. Cosmol. Astropart. Phys.* **10** (2017) 046.
- [55] M. Biagetti, G. Franciolini, A. Kehagias, and A. Riotto, *J. Cosmol. Astropart. Phys.* **07** (2018) 032.
- [56] J. M. Ezquiaga, J. García-Bellido, and V. Vennin, *J. Cosmol. Astropart. Phys.* **03** (2020) 029.
- [57] C. Pattison, V. Vennin, D. Wands, and H. Assadullahi, *J. Cosmol. Astropart. Phys.* **04** (2021) 080.
- [58] D. G. Figueroa, S. Raatikainen, S. Rasanen, and E. Tomberg, *J. Cosmol. Astropart. Phys.* **05** (2022) 027.
- [59] M. H. Namjoo, H. Firouzjahi, and M. Sasaki, *Europhys. Lett.* **101**, 39001 (2013).
- [60] X. Chen, H. Firouzjahi, E. Komatsu, M. H. Namjoo, and M. Sasaki, *J. Cosmol. Astropart. Phys.* **12** (2013) 039.
- [61] Y.-F. Cai, X. Chen, M. H. Namjoo, M. Sasaki, D.-G. Wang, and Z. Wang, *J. Cosmol. Astropart. Phys.* **05** (2018) 012.
- [62] S. Passaglia, W. Hu, and H. Motohashi, *Phys. Rev. D* **99**, 043536 (2019).
- [63] M. Biagetti, V. De Luca, G. Franciolini, A. Kehagias, and A. Riotto, *Phys. Lett. B* **820**, 136602 (2021).
- [64] V. Atal and C. Germani, *Phys. Dark Universe* **24**, 100275 (2019).
- [65] V. Atal, J. Garriga, and A. Marcos-Caballero, *J. Cosmol. Astropart. Phys.* **09** (2019) 073.
- [66] M. Taoso and A. Urbano, *J. Cosmol. Astropart. Phys.* **08** (2021) 016.
- [67] S. Young, *J. Cosmol. Astropart. Phys.* **05** (2022) 037.
- [68] C. T. Byrnes, P. S. Cole, and S. P. Patil, *J. Cosmol. Astropart. Phys.* **06** (2019) 028.

- [69] S. M. Leach, M. Sasaki, D. Wands, and A. R. Liddle, *Phys. Rev. D* **64**, 023512 (2001).
- [70] D. Wands, *Phys. Rev. D* **60**, 023507 (1999).
- [71] G. Franciolini, I. Musco, P. Pani, and A. Urbano, [arXiv:2209.05959](https://arxiv.org/abs/2209.05959).
- [72] M. Y. Khlopov and A. G. Polnarev, *Phys. Lett.* **97B**, 383 (1980).
- [73] A. M. Green, A. R. Liddle, and A. Riotto, *Phys. Rev. D* **56**, 7559 (1997).
- [74] I. Musco and J. C. Miller, *Classical Quantum Gravity* **30**, 145009 (2013).
- [75] T. Harada, C.-M. Yoo, K. Kohri, K.-i. Nakao, and S. Jhingan, *Astrophys. J.* **833**, 61 (2016).
- [76] B. Carr, T. Tenkanen, and V. Vaskonen, *Phys. Rev. D* **96**, 063507 (2017).
- [77] B. Carr, K. Dimopoulos, C. Owen, and T. Tenkanen, *Phys. Rev. D* **97**, 123535 (2018).
- [78] A. Escrivà, C. Germani, and R. K. Sheth, *J. Cosmol. Astropart. Phys.* **01** (2021) 030.
- [79] E. de Jong, J. C. Aurekoetxea, and E. A. Lim, *J. Cosmol. Astropart. Phys.* **03** (2022) 029.
- [80] V. De Luca, G. Franciolini, A. Kehagias, P. Pani, and A. Riotto, *Phys. Lett. B* **832**, 137265 (2022).
- [81] K. Inomata, K. Kohri, T. Nakama, and T. Terada, *Phys. Rev. D* **100**, 043532 (2019).
- [82] K. Inomata, K. Kohri, T. Nakama, and T. Terada, *J. Cosmol. Astropart. Phys.* **10** (2019) 071.
- [83] G. Domènech, *Int. J. Mod. Phys. D* **29**, 2050028 (2020).
- [84] G. Domènech, S. Pi, and M. Sasaki, *J. Cosmol. Astropart. Phys.* **08** (2020) 017.
- [85] A. Hook, G. Marques-Tavares, and D. Racco, *J. High Energy Phys.* **02** (2021) 117.
- [86] K. Saikawa and S. Shirai, *J. Cosmol. Astropart. Phys.* **05** (2018) 035.
- [87] S. Young, I. Musco, and C. T. Byrnes, *J. Cosmol. Astropart. Phys.* **11** (2019) 012.
- [88] V. De Luca, G. Franciolini, A. Kehagias, M. Peloso, A. Riotto, and C. Ünal, *J. Cosmol. Astropart. Phys.* **07** (2019) 048.
- [89] C. Germani and I. Musco, *Phys. Rev. Lett.* **122**, 141302 (2019).
- [90] A. Escrivà and A. E. Romano, *J. Cosmol. Astropart. Phys.* **05** (2021) 066.
- [91] I. Musco, S. Young, and K. Jedamzick (to be published).
- [92] I. Musco, *Phys. Rev. D* **100**, 123524 (2019).
- [93] I. Musco, V. De Luca, G. Franciolini, and A. Riotto, *Phys. Rev. D* **103**, 063538 (2021).
- [94] C. T. Byrnes, M. Hindmarsh, S. Young, and M. R. S. Hawkins, *J. Cosmol. Astropart. Phys.* **08** (2018) 041.
- [95] A. M. Green and B. J. Kavanagh, *J. Phys. G* **48**, 043001 (2021).
- [96] <https://github.com/bradkav/PBHbounds>
- [97] A. K. Saha and R. Laha, *Phys. Rev. D* **105**, 103026 (2022).
- [98] R. Laha, *Phys. Rev. Lett.* **123**, 251101 (2019).
- [99] A. Ray, R. Laha, J. B. Muñoz, and R. Caputo, *Phys. Rev. D* **104**, 023516 (2021).
- [100] S. Mittal, A. Ray, G. Kulkarni, and B. Dasgupta, *J. Cosmol. Astropart. Phys.* **03** (2022) 030.
- [101] S. Clark, B. Dutta, Y. Gao, L. E. Strigari, and S. Watson, *Phys. Rev. D* **95**, 083006 (2017).
- [102] R. Laha, J. B. Muñoz, and T. R. Slatyer, *Phys. Rev. D* **101**, 123514 (2020).
- [103] J. Berteaud, F. Calore, J. Iguaz, P. D. Serpico, and T. Siegert, *Phys. Rev. D* **106**, 023030 (2022).
- [104] W. DeRocco and P. W. Graham, *Phys. Rev. Lett.* **123**, 251102 (2019).
- [105] M. Boudaud and M. Cirelli, *Phys. Rev. Lett.* **122**, 041104 (2019).
- [106] B. J. Carr, K. Kohri, Y. Sendouda, and J. Yokoyama, *Phys. Rev. D* **81**, 104019 (2010).
- [107] H. Niikura *et al.*, *Nat. Astron.* **3**, 524 (2019).
- [108] P. Tisserand *et al.* (EROS-2 Collaboration), *Astron. Astrophys.* **469**, 387 (2007).
- [109] H. Niikura, M. Takada, S. Yokoyama, T. Sumi, and S. Masaki, *Phys. Rev. D* **99**, 083503 (2019).
- [110] M. Oguri, J. M. Diego, N. Kaiser, P. L. Kelly, and T. Broadhurst, *Phys. Rev. D* **97**, 023518 (2018).
- [111] P. D. Serpico, V. Poulin, D. Inman, and K. Kohri, *Phys. Rev. Res.* **2**, 023204 (2020).
- [112] B. P. Abbott *et al.* (LIGO Scientific, Virgo Collaborations), *Phys. Rev. Lett.* **123**, 161102 (2019).
- [113] B. J. Kavanagh, D. Gaggero, and G. Bertone, *Phys. Rev. D* **98**, 023536 (2018).
- [114] K. W. K. Wong, G. Franciolini, V. De Luca, V. Baibhav, E. Berti, P. Pani, and A. Riotto, *Phys. Rev. D* **103**, 023026 (2021).
- [115] G. Hütsi, M. Raidal, V. Vaskonen, and H. Veermäe, *J. Cosmol. Astropart. Phys.* **03** (2021) 068.
- [116] V. De Luca, G. Franciolini, P. Pani, and A. Riotto, *J. Cosmol. Astropart. Phys.* **05** (2021) 003.
- [117] G. Franciolini, V. Baibhav, V. De Luca, K. K. Y. Ng, K. W. K. Wong, E. Berti, P. Pani, A. Riotto, and S. Vitale, *Phys. Rev. D* **105**, 083526 (2022).
- [118] S. Sugiyama, V. Takhistov, E. Vitagliano, A. Kusenko, M. Sasaki, and M. Takada, *Phys. Lett. B* **814**, 136097 (2021).
- [119] N. Esser and P. Tinyakov, [arXiv:2207.07412](https://arxiv.org/abs/2207.07412).
- [120] F. Capela, M. Pshirkov, and P. Tinyakov, *Phys. Rev. D* **87**, 123524 (2013).
- [121] F. Capela, M. Pshirkov, and P. Tinyakov, *Phys. Rev. D* **87**, 023507 (2013).
- [122] F. Capela, M. Pshirkov, and P. Tinyakov, *Phys. Rev. D* **90**, 083507 (2014).
- [123] P. Montero-Camacho, X. Fang, G. Vasquez, M. Silva, and C. M. Hirata, *J. Cosmol. Astropart. Phys.* **08** (2019) 031.
- [124] A. Moradinezhad Dizgah, G. Franciolini, and A. Riotto, *J. Cosmol. Astropart. Phys.* **11** (2019) 001.
- [125] V. De Luca, G. Franciolini, and A. Riotto, *Phys. Lett. B* **807**, 135550 (2020).
- [126] I. Dalianis, G. P. Kodaxis, I. D. Stamou, N. Tetradis, and A. Tsigkas-Kouvelis, *Phys. Rev. D* **104**, 103510 (2021).
- [127] P. S. Cole, A. D. Gow, C. T. Byrnes, and S. P. Patil, [arXiv:2204.07573](https://arxiv.org/abs/2204.07573).
- [128] S. Clesse and J. Garcia-Bellido, *Phys. Dark Universe* **38**, 101111 (2022).
- [129] K. K. Y. Ng, G. Franciolini, E. Berti, P. Pani, A. Riotto, and S. Vitale, *Astrophys. J. Lett.* **933**, L41 (2022).
- [130] M. Martinelli, F. Scarcella, N. B. Hogg, B. J. Kavanagh, D. Gaggero, and P. Fleury, *J. Cosmol. Astropart. Phys.* **08** (2022) 006.

- [131] R. Abbott *et al.* (LIGO Scientific, Virgo, KAGRA Collaborations), [arXiv:2111.03634](#).
- [132] A. M. Farah, M. Fishbach, R. Essick, D. E. Holz, and S. Galaudage, *Astrophys. J.* **931**, 108 (2022).
- [133] J. R. Espinosa, D. Racco, and A. Riotto, *J. Cosmol. Astropart. Phys.* **09** (2018) 012.
- [134] K. Kohri and T. Terada, *Phys. Rev. D* **97**, 123532 (2018).
- [135] N. Bartolo, V. De Luca, G. Franciolini, M. Peloso, D. Racco, and A. Riotto, *Phys. Rev. D* **99**, 103521 (2019).
- [136] N. Bartolo, V. De Luca, G. Franciolini, A. Lewis, M. Peloso, and A. Riotto, *Phys. Rev. Lett.* **122**, 211301 (2019).
- [137] S. Balaji, J. Silk, and Y.-P. Wu, *J. Cosmol. Astropart. Phys.* **06** (2022) 008.
- [138] V. Vaskonen and H. Veermäe, *Phys. Rev. Lett.* **126**, 051303 (2021).
- [139] H. Middleton, A. Sesana, S. Chen, A. Vecchio, W. Del Pozzo, and P. A. Rosado, *Mon. Not. R. Astron. Soc.* **502**, L99 (2021).
- [140] E. Thrane and J. D. Romano, *Phys. Rev. D* **88**, 124032 (2013).
- [141] S. S. Bavera, G. Franciolini, G. Cusin, A. Riotto, M. Zevin, and T. Fragos, *Astron. Astrophys.* **660**, A26 (2022).
- [142] R. M. Shannon *et al.*, *Science* **349**, 1522 (2015).
- [143] G. Janssen *et al.*, *Proc. Sci. AASKA14* (2015) 037.
- [144] K. T. Abe, Y. Tada, and I. Ueda, *J. Cosmol. Astropart. Phys.* **06** (2021) 048.
- [145] C. Yuan and Q.-G. Huang, *Phys. Lett. B* **821**, 136606 (2021).
- [146] P. Adshead, K. D. Lozanov, and Z. J. Weiner, *J. Cosmol. Astropart. Phys.* **10** (2021) 080.
- [147] K. T. Abe, R. Inui, Y. Tada, and S. Yokoyama, [arXiv:2209.13891](#).
- [148] Z. Chang, X. Zhang, and J.-Z. Zhou, [arXiv:2209.12404](#).
- [149] K. A. Malik and D. Wands, *J. Cosmol. Astropart. Phys.* **02** (2005) 007.
- [150] S. Geller, W. Qin, E. McDonough, and D. I. Kaiser, *Phys. Rev. D* **106**, 063535 (2022).
- [151] O. Özsoy and G. Tasinato, *Phys. Rev. D* **105**, 023524 (2022).
- [152] S. Balaji, H. V. Ragavendra, S. K. Sethi, J. Silk, and L. Sriramkumar, [arXiv:2206.06386](#).
- [153] G. Franciolini, R. Cotesta, N. Loutrel, E. Berti, P. Pani, and A. Riotto, *Phys. Rev. D* **105**, 063510 (2022).
- [154] G. Rakavy and G. Shaviv, *Astrophys. J.* **148**, 803 (1967).
- [155] Z. Barkat, G. Rakavy, and N. Sack, *Phys. Rev. Lett.* **18**, 379 (1967).
- [156] G. S. Fraley, *Astrophys. Space Sci.* **2**, 96 (1968).
- [157] S. E. Woosley, *Astrophys. J.* **836**, 244 (2017).
- [158] R. Farmer, M. Renzo, S. E. de Mink, P. Marchant, and S. Justham, [arXiv:1910.12874](#).
- [159] R. Abbott *et al.* (LIGO Scientific, Virgo Collaborations), *Phys. Rev. Lett.* **125**, 101102 (2020).
- [160] V. De Luca, V. Desjacques, G. Franciolini, P. Pani, and A. Riotto, *Phys. Rev. Lett.* **126**, 051101 (2021).
- [161] G. Franciolini, A. Maharana, and F. Muia, *Phys. Rev. D* **106**, 103520 (2022).